

# 15 $\mu$ m ISO<sup>1</sup> observations of the 1415+52 CFRS field: the cosmic star formation rate as derived from deep UV, optical, mid-IR and radio photometry

H. Flores<sup>1,9</sup>, F. Hammer<sup>1,9</sup>, T.X. Thuan<sup>2</sup>, C. Césarsky<sup>3</sup>, F.X. Desert<sup>4</sup>, A. Omont<sup>5</sup>, S.J. Lilly<sup>6</sup>, S. Eales<sup>7</sup>, D. Crampton<sup>8</sup> and O. Le Fèvre<sup>1</sup>

1) Observatoire de Paris, Section de Meudon, DAEC, 92195 Meudon Principal Cedex, France.

2) Astronomy Department, University of Virginia, USA.

3) Service d'Astrophysique, CEA, France.

4) Institut d'Astrophysique Spatiale, Orsay. France.

5) Institut d'Astrophysique de Paris, France.

6) Department of Astronomy, University of Toronto, Toronto, Canada.

7) University of Cardiff, UK.

8) Dominion Astrophysical Observatory, National Research Council of Canada, Victoria, Canada

Received 09 June 1988; accepted 11 November 1988

to appear in Ap.J.

---

<sup>1</sup>Based on observations with ISO, an ESA project with instruments funded by ESA Member States" (especially the PI countries: France, Germany, the Netherlands and the United Kingdom) with the participation of ISAS and NASA

<sup>9</sup>Visiting Astronomer, Canada-France-Hawaii Telescope (CFHT), which is operated by the National Research Council of Canada, the Centre de Recherche Scientifiques of France, and the University of Hawaii.

## ABSTRACT

The CFRS 1452+52 field has been deeply imaged with the Infrared Space Observatory (ISO) using ISOCAM through the LW3 filter (12-18 $\mu$ m). Careful data analysis and comparison to deep optical and radio data have allowed us to generate a catalog of 78 15  $\mu$  sources with both radio and optical identifications. They are redder and lie at higher redshift than I-band selected galaxies, with most of them being star-forming galaxies.

We have considered the galaxies detected at radio and 15 $\mu$ m wavelengths which potentially include all strong and heavily extinguished starbursts, up to  $z=1$ . Spectral energy distributions (SED) for each of the sources have been derived using deep radio, mid-IR, near-IR, optical and UV photometry. The sources were then spectrally classified by comparing to SEDs of well known nearby galaxies. By deriving their FIR luminosities by interpolation, we can estimate their Star Formation Rate (SFR) in a way which does not depend sensitively on the extinction. 75% (-40%, +10%) of the star formation at  $z \leq 1$  is related to IR emission and the global extinction is in the range  $A_V=0.5 - 0.85$ . While heavily extinguished starbursts, with SFR in excess of  $100 \text{ M}_\odot \text{yr}^{-1}$  constitute less than a percent of all galaxies, they contribute about 18% of the SFR density out to  $z=1$ . Their morphologies range from S0 to Sab, and more than a third are interacting systems.

The SFR derived by FIR fluxes is likely to be  $\sim 2.9$  times higher than those previously estimated from UV fluxes. The derived stellar mass formed since the redshift of 1 could be too high when compared to the present day stellar mass density. This might be due to an IMF in distant star-forming galaxies different

from the solar neighborhood one, or to an underestimate of the local stellar mass density.

*Subject headings:* galaxies: catalogue, active; galaxies: observations; infrared: galaxies

## 1. Introduction

The 2800Å and [OII]3727 emission line luminosity densities have decreased by a factor of  $\sim 10$  from  $z = 1$  to the present day (Lilly et al. 1996; Hammer et al. 1997). This has led Madau et al. (1996, 1998) to suggest that the cosmic star formation density has decreased by the same factor within that redshift interval, and that most of the stars seen now were formed during the first half of the Universe’s existence. The UV emission from galaxies is produced by a complex mix of short and moderately long-lived stars, the latter (late B and A0 stars) contributing more at longer UV wavelengths. Even old stars in luminous early-type and quiescent galaxies can contribute to the observed UV luminosity density. However the most important uncertainty in estimating the star formation density from the UV luminosity density is due to the extinction which can show large variations from one galaxy to another. For example in IRAS star-forming galaxies, most of the energy is reemitted at far-IR (FIR) wavelengths and these objects are either missed or their star formation rates are severely underestimated when derived by UV measurements. This is why it is often thought that the UV luminosity density is likely to provide only a lower limit to the actual star formation density. The situation is complicated further by the expected contamination by AGN to the UV light density.

In an attempt to better estimate the cosmic star formation density, Tresse and Maddox (1998) have calculated the extinction-corrected  $H\alpha$  luminosity density at  $z \sim 0.2$ . Their result is in agreement with the UV (2800Å) at  $z = 0.35$  (Lilly et al, 1996) if an extinction of 1 mag is assumed for the UV continuum. A preliminary study of more distant galaxies indicates that the situation might be similar at  $z \sim 1$  (Glazebrook et al, 1998), but it is limited by the difficulty of measuring the near-IR redshifted  $H\alpha$  line of faint galaxies with 4m telescopes.

Multi-wavelength analyses can provide, in principle, a detailed budget of the energy output in each wavelength range for the entire galaxy energy distribution. It has been shown for

local galaxies that FIR luminosities are tightly correlated with radio luminosities (Helou et al. 1987; Condon 1992), and that bolometric luminosities are most closely proportional to 12  $\mu\text{m}$  luminosities (Spinoglio and Malkan, 1989; Spinoglio et al, 1995). These trends hold over a wide range of galaxy luminosities, despite the large variety of galaxy energy distributions. Only AGNs which are believed to be associated to supermassive black holes, appear not to follow those relations (Condon et al. 1988).

Recent observational advances allow now to study distant galaxies from the UV to the radio, sampling a wavelength range which covers most of the domain where their energy is being emitted. VLA deep surveys are able to detect sources down to 10  $\mu\text{Jy}$  (e.g. the 5GHz surveys of Fomalont et al. 1992 and Richards et al. 1998) and ISOCAM (Césarky *et al.* 1996) aboard the Infrared Space Observatory (ISO, Kessler *et al.* 1996) can reach detection limits of 100  $\mu\text{Jy}$  at 15  $\mu\text{m}$  (Elbaz et al. 1998). In the range 60–200  $\mu\text{m}$  the detection limits are 0.2 Jy at 60  $\mu\text{m}$  from the IRAS Faint Source Catalog (Moshir et al. 1989) and 0.1 Jy at 175  $\mu\text{m}$  from the FIRBACK survey carried out with ISO (Clements et al. 1998; Puget et al. 1998). FIR detections thus appear to be not sensitive enough to reach the same depth as radio and Mid-IR (MIR) deep surveys. For example, if we consider a strong and highly reddened starburst (SBH in the terminology of Schmitt et al. 1998), a  $S_{15\mu\text{m}}=250$   $\mu\text{Jy}$  source would correspond to a 0.009 Jy source at 60  $\mu\text{m}$ , and a  $z=1$  redshifted SBH with  $S_{5\text{GHz}}=16\mu\text{Jy}$  would have 0.022 Jy at 175  $\mu\text{m}$ .

The sensibility and high spatial resolution of ISOCAM allow the study of distant field galaxies at MIR wavelengths ( $2 \leq \lambda \leq 20\mu\text{m}$ ). Star-forming galaxies and AGN are easily detectable in the wavelength range 5–18  $\mu\text{m}$ , even at large distances (Franceschini 1991). The Canada-France Redshift Survey (CFRS) field at 1415+52 (Lilly et al. 1995a) is the second most observed field at all wavelengths after the Hubble Deep Field (HDF). While it does not go as deep, it is  $\sim 18.5$  larger in area and thus is more suited for source statistics when a volume-limited ( $z \leq 1$ ) sample is considered. It has been observed to very faint

magnitudes in the BVIK bands (photometric completeness down to  $I_{AB}=23.5$  mag, Lilly *et al.* 1995b), possesses spectroscopic data for galaxies brighter than  $I_{AB} = 22.5$  mag from the CFRS, and deep radio observations ( $S_{5GHz} \geq 16 \mu\text{Jy}$ , Fomalont *et al.* 1992). The CFRS sample can be considered complete in the sense that it contains all luminous ( $M_B(AB) \leq -20.5$ ) galaxies in the volume out to  $z = 1$ .

This paper presents a major follow-up study of the above CFRS field, by gathering and studying representative samples of galaxies selected at radio and MIR wavelengths. With sensitivity limits of  $250\mu\text{Jy}$  at  $15\mu\text{m}$  (ISOCAM) and  $16\mu\text{Jy}$  at  $5\text{GHz}$  (VLA), these samples should include all strong and reddened starbursts up to  $z=1$ , with star formation rates larger than  $100$  and  $70 M_\odot \text{ yr}^{-1}$  respectively. These samples should not miss any luminous FIR source in the CFRS field as the sources were selected using observations which cover wavelengths on either side of the  $60\text{-}100\mu\text{m}$  bump. They can thus be used ultimately to estimate the star formation density which has been missed by UV flux measurements.

The nature of the  $\mu\text{Jy}$  radio sources in the field and of their optical counterparts has been extensively discussed by Hammer *et al.* (1995). Recently this field has been imaged by ISOCAM in the LW2 ( $5\text{-}8.5\mu\text{m}$ ) and LW3 ( $12\text{-}18\mu\text{m}$ ) filters. We have presented the  $6.75\mu\text{m}$  LW2 observations in a previous paper (Flores *et al.* 1998). There, we have discussed the details of the data reduction, the astrometry and the confidence level for each source. Fifty four sources with  $S/N \geq 3$  were detected with  $S_{6.7\mu\text{m}} \geq 150 \mu\text{Jy}$ , 21 of which possess spectra from the CFRS. Of the latter, 7 were stars. Among the non-stellar sources, 42% were classified as AGN and 50% as  $S + A$  galaxies, i.e. star-forming galaxies with a significant population of A stars. The relatively high fraction of AGN is not unexpected because strong AGN are generally associated with a hot dust component and have generally bluer near-IR colors than starbursts. While the  $6.75\mu\text{m}$  data appears not to be optimal for selecting starbursts, they are useful for constraining galaxy SEDs, as galaxies (and especially Seyfert

2 galaxies) show large variations in their MIR color properties.

We present here the  $15\mu\text{m}$  LW3 observations. For galaxies in the redshift range  $0.25 \leq z \leq 1$ , this filter samples the  $8\text{-}12\mu$  rest wavelength region. It can thus simultaneously provide samples of normal, starburst and active galaxies which are complete to a well-defined bolometric flux limit (Spinoglio et al., 1995). MIR measurements are sensitive to dust thermal emission ( $\lambda > 5\mu\text{m}$ ), its broad emission being interpreted as due to PAHs or Unidentified Infrared Bands (UIBs) carriers ( $3\mu\text{m} < \lambda < 18\mu\text{m}$ ), and to nuclear non-thermal radiation. There have been recent suggestions that PAHs arise from photo-dissociation regions around HII regions, the latter showing red near-IR continua (Laurent and Mirabel, 1998, in preparation). Genzel et al. (1998) have used the relative strengths of PAH features and near-IR colors to discriminate AGN dominated objects from starbursts. Lutz et al. (1998) found that the fraction of AGN powered objects is relatively small at moderate IR luminosities (typically  $L_{IR} < 2 \cdot 10^{12}L_{\odot}$ ), but reaches half at higher luminosities. In section 2, we discuss the data reduction, the astrometry and the construction of the catalogs. In section 3 we present the redshift distribution of the ISOCAM LW3 objects, and their optical properties including their morphologies from HST images. Section 4 presents spectral energy distributions from UV to radio wavelengths and a classification scheme for these and for radio-selected galaxies. Derivations of the UV and IR luminosity densities are presented in Section 5. Section 6 describes the global star formation density at  $z \leq 1$  and compares it to previous estimates based on the UV luminosity density.

## 2. Observations and data reduction

The CFRS field at  $1415+52$  was mapped with the ISOCAM LW channel (PFOV 6 arcsec pixel) and the filter LW3 ( $12\text{-}18\mu\text{m}$ ). Twelve individual images were obtained using the micro-scanning AOT mode (CAM01) and resulting in a total integration time of  $\sim 1200$

sec pixel<sup>-1</sup>. The micro-scanning mode provides the best spatial resolution by superposition of images. The same pixel of the sky was placed in different parts of the camera in order to minimize and detect any systematic effects. The micro-scanning AOT technique also allows an accurate flat-field image to be generated and yields a pixel size of 1''.5 in the final integrated image. The detection and removal of transients and glitches, integration of images, absolute flux calibration, and source detection were carried out using the method described by Désert *et al.* (1998). This method has been found to be particularly well adapted to our observational strategy, i.e. coadding the twelve images, without redundancy within each image. Special attention was paid to possible error propagation in the flux values. The photometric accuracy has been discussed by Desert *et al.* (1998). From the stellar energy distributions, we find the photometry to be accurate to a few percent for sources with S/N > 10, and to  $\sim$ 50% for sources with S/N = 3.

Figure 1 displays the final 15 $\mu$ m image of the CFRS 1415+52 field. Individual images were carefully registered with each other in order to optimize the image quality of the brightest compact objects (see Flores *et al.*, 1998). The final image of the whole ISO field has a resolution equivalent to a median FWHM $\sim$ 11'' (calculated with DAOPHOT under IRAF). It can be seen that the noise structure (Figure 1) is relatively homogeneous (the standard deviation is lower than one tenth of the mean) in  $\sim$  85% of the area of the image, except near the edges.

Figure 1 ; Flores et al. , 1998

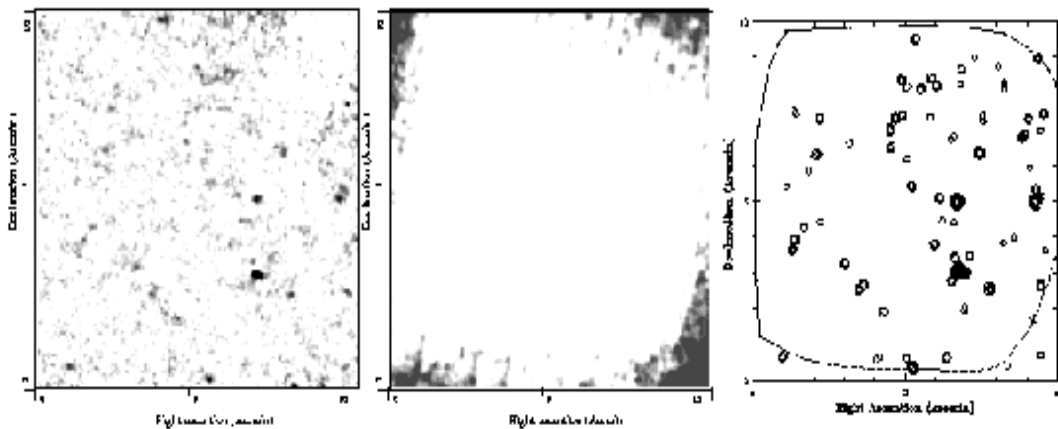


Fig. 1.— At left is the combined LW3 (12-18 $\mu$ m) image of the whole 10'x10' CFRS 1415+52 field. Center coordinates are  $\alpha$ (2000)= 14 17 53.7 and  $\delta$ (2000)= 52 30 30.7. The scale is 1.5" per pixel. The image has a FWHM resolution of  $\sim$ 11" and the scale is 1".5 per pixel. In the middle is shown the map of noise. In 85% of the map, the noise is within 10% of the average. At right are shown the locations of the catalogued 15 $\mu$ m sources which have successfully passed our selection criteria (see text). Sources with S/N= 3 are represented by a single circle, while sources with S/N= 4, 6 and 8 are shown by 2, 3 and 4 concentric circles.

Point sources are iteratively extracted with a Gaussian PSF of 9 arcsecond FWHM; a correction factor of 1.39 (deduced from a detailed modelling of the effective ISO PSF, Cesarsky *et al.*, 1996) is applied to the measured flux (calibrated with ISOCAM user’s manual conversion table) to account for losses in the wings of the true PSF.

## 2.1. ISO source catalogues

Source detections were made on the basis of S/N and repeatability in three independent combinations of the 12 individual images (for details about the source detection repeatability and classification, see F.X. Desert *et al.* 1998). The repeatability test is based on the redundancy factor, which is the number of times that the sky pixel was seen by different pixels on the camera. The software built three independent projection subrasters, and for each source candidate the flux and error are measured at the same position in each subrasters. The quality factor is based on flux measurements and varies from the best confidence index ( $= 4$ ) to the worse confidence level ( $= 0$ , see eqs. 7 to 11 of Désert *et al.*, 1998). We have considered only sources with a confidence level higher than 3, which means that the final source flux is within  $3\sigma$  ( $2\sigma$  in the case of 4) of the source fluxes in subrasters, where  $\sigma$  is the error in the final source flux.

Altogether, 78 sources with  $S/N \geq 3$  fulfill these detection criteria (Table 1). We have considered as secure detections those sources with  $S/N \geq 4$  (41 sources, catalogs 1, 2 and 3). The 37 sources listed in catalogs 4, 5 and 6 with  $3 < S/N < 4$  are considered “less” secure. That a  $S/N \geq 4$  is a good detection criterion is confirmed by studies in the Lockman Hole Deep Survey (Césarsky *et al.* 1998, in prep) which show that sources with  $S/N \geq 4$  in individual frames are confirmed in 95% of cases in the final integrated image ( $S/N > 10$ ).

Figure 2 ; Flores et al. 1998

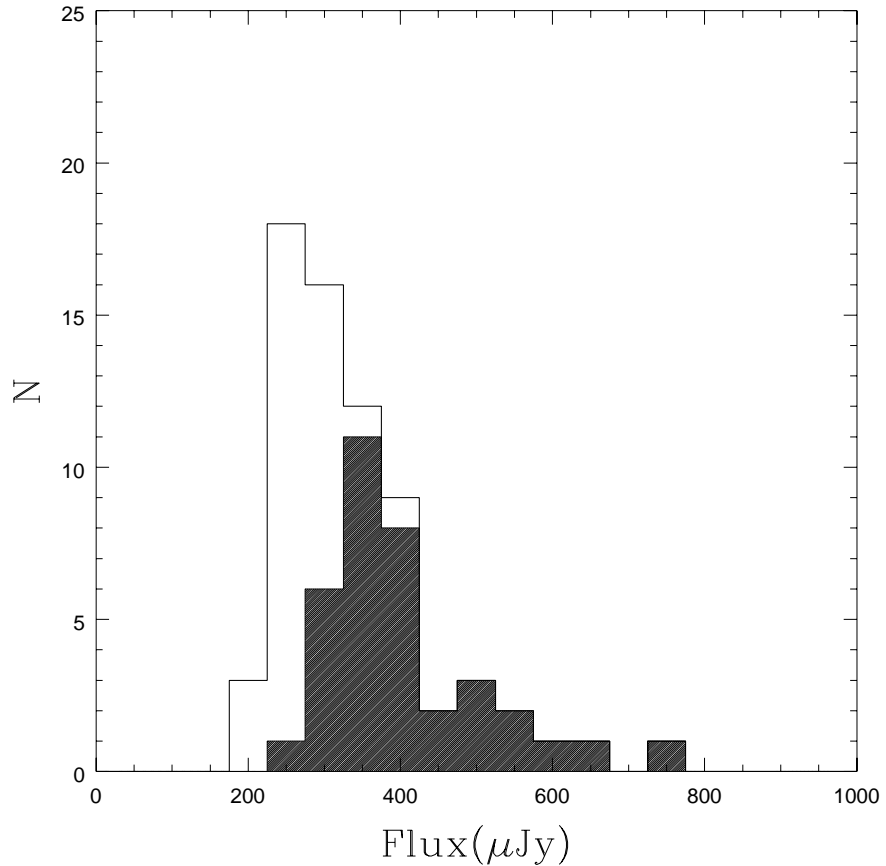


Fig. 2.— The flux distribution of ISOCAM 12–18 micron sources. Sources with  $S/N > 4$  (catalogs 1 & 2) are shown by the shaded histogram.

Fig. 3.—  $(I-K)_{AB}$  color distribution of  $15\mu\text{m}$  sources with  $I_{AB} \leq 22.5$  (bottom panel) compared to the CFRS galaxy color distribution (top panel).

Figure 2 shows the flux distribution and the comparison to results from other fields suggests a completeness down to  $\sim 350 \mu\text{Jy}$  for sources with  $\text{S/N} \geq 4$ , and to  $\sim 250 \mu\text{Jy}$  for sources with  $\text{S/N} \geq 3$ , at least for the central 85% of the  $10' \times 10'$  field. These correspond to number densities of 1590 sources per square degree, for  $S_{15\mu\text{m}} \geq 350 \mu\text{Jy}$ , slightly larger than the number density of 1260 source per square degree found by Elbaz et al. (1998) in their ISOCAM survey of the Hubble Deep Field.

Surveys of low S/N ratio sources can be affected by several biases, the main ones being the possible unreliability of sources near the survey limit and the Eddington bias. Near the flux density limit, completeness falls off and possible false sources may be introduced. The fraction of false sources can be controlled through a random match control test based on the identification rate of ISOCAM sources with optical sources (see next section) and should be small. We have checked whether our higher number count relative to the HDF data could be due to the Eddington bias. Our survey is intermediate in depth between the Lockman Hole Deep survey (from 450 to 1400 microJy) and the Hubble Deep Field survey (from 125 to 350 microJy). Elbaz et al. (1998) quote a slope of 1.3 and 2.1 for the HDF and Lockman Hole respectively, and we should expect an intermediate slope near  $\sim 1.7$ , lower than the value of 2.2 derived from our  $S \geq 250$  and  $S \geq 350 \mu\text{Jy}$  counts. We have attempted to estimate the fraction of sources which may have entered our sample erroneously because statistical uncertainties bring them over the detection threshold, while they actually possess a lower flux density than  $S=250$  microJy. We have adopted a slope of 1.7 and perform Monte Carlo simulations of 30 000 sets, assuming a gaussian distribution for the noise of faint sources. The simulations show that  $\sim 15\%$  of the sources with  $\text{S/N} \geq 3$  can be sources with fluxes lower than 250 microJy, but that fraction drops to only  $\sim 2\%$  for sources with  $\text{S/N} \geq 4$ . This is probably close to the truth since after accounting for the Eddington bias (i.e. removing 15% of the 78 sources with  $\text{S/N} > 3$  as well as 2% of the 41  $\text{S/N} > 4$  sources), the slope becomes 1.7, in good agreement with other surveys.

Biases in source counts thus affect mainly the faintest sources in our sample (those with  $3 \leq S/N < 4$ ). They are the least powerful sources, and as such cannot introduce significant uncertainties on global luminosity density estimates.

## 2.2. Astrometry and counterparts at radio and optical wavelengths

The positional accuracy of ISO sources is affected by both the pixel size and the distortion (see Flores et al, 1998). The superposition of the ISOCAM field onto the CFRS 1415+52 optical field was done by matching the positions of the 6 brightest sources (which were also detected at  $6.75\mu\text{m}$ ). By comparing the astrometry of the optical and ISOCAM LW3 sources, we find a median difference of  $\sim 3.7$  arcsec. This is reasonable given that the ISO pixel size is  $\sim 6.0$  arcsec.

The astrometric accuracy of the CFRS 1415+52 optical field is  $0''.15$ , based on the comparison between the optical and radio frames (Hammer *et al.*, 1995). We first compare the  $15\mu\text{m}$  image with the VLA  $\mu\text{Jy}$  radio map (Fomalont et al, 1991), and calculate the probability of a pure coincidence, assuming Poisson statistics:

$$P(d, S_{5\text{GHz}}) = 1 - e^{-n(S_{5\text{GHz}})\pi d^2} \quad (1)$$

where  $d$  is the angular distance between the ISOCAM LW3 source and the radio source in degrees and  $n$  is the integrated density of radiosources with flux  $S_{5\text{GHz}}$  ( $dn(S_{5\text{GHz}}) = 83520 S_{5\text{GHz}}^{-1.18} dS$ ). Ten ISOCAM LW3 sources are thus identified (see Table 1). They all possess optical counterparts (Hammer *et al.* 1995).

Astrometry of ISOCAM LW3 sources not detected in radio has been derived by comparison to the optical sources in the CFRS 1415+52 field, and

$$P(d, I_{AB}) = 1 - e^{-n(I_{AB})\pi d^2} \quad (2)$$

is the probability of a pure coincidence, where  $n(I_{AB})$  are integrated counts derived from the CFRS. In table 1, six catalogs have been defined with different S/N values ( $3 \leq S/N \leq 4, S/N > 4$ ) and P values ( $P < 0.02, P > 0.02$ , and sources without optical counterparts within 12 arcsec). Objects which are also radio sources are indicated. These all have very low probabilities of accidental coincidence.

We also compare the  $15\mu\text{m}$  map with that described in Flores et al. (1998) at  $6.75\mu\text{m}$ . We found 17 of the 78  $15\mu\text{m}$  sources to be also detected at  $6.75\mu\text{Jy}$  (with flux densities above  $150\mu\text{Jy}$ ). The fraction of  $15\mu\text{m}$  sources also detected at  $6.75\mu\text{m}$  increases with S/N (see Table 2).

The final noise structure in ISOCAM images is not strictly gaussian, because of possible residuals glitches, and because the  $15\mu\text{m}$  positions could not have been fully corrected for image distortions. To calibrate the probabilities given in Table 1 in an empirical way, we have applied a random match control test to the ISOCAM image by rotating it successively by 45, 90, 180 and 270 degrees relative to the optical image. Only  $3 \pm 1$  of the 78 ISOCAM sources were found to be randomly associated with an optical counterpart with  $I_{AB} < 22.5$  and  $P < 0.02$ . This should be compared to the 37  $I_{AB} < 22.5$  and  $P < 0.02$  counterparts found in Table 1. These experiments suggest that non-gaussian effects cannot affect our probability calculations by more than a factor 2.

Table 1 lists the sources in six catalogs, the confidence level decreasing in each successive catalog. The ISOCAM LW3 sources and their optical counterparts are given in columns (1) & (2). Column (3) provides the optical source redshift when available, "star" indicates that the ISO source is stellar, while "—" indicates that no redshift is available. In columns (4), (5) and (6) are the I, V and K isophotal magnitudes in the AB system, and "—" indicates that no photometry is available. Column (7) gives the angular distance in arcsec between the ISOCAM LW3 source and optical (or radio) identification, while column (8) gives the associated probability of coincidence. Columns (9) and (10) give the flux density at 12–18  $\mu\text{m}$  and its error in  $\mu\text{Jy}$ . The positions and flux densities of the 9 non-identified ISO sources are also listed in Table 1 (catalogues 3 and 6).

Among the sources with  $S/N \geq 4$ , only 8 (19%) have counterparts fainter than  $I_{AB} = 22.5$ , or no optical counterparts. These sources could be at redshifts higher than 1. The fraction of very faint optical counterparts increases for the fainter ISOCAM LW3 sources (41% for sources with  $3 < S/N < 4$ ), which is to be expected. On the other hand, in the most uncertain catalog (catalog 5), one can expect  $\sim 4.6$  sources out of 19 to be pure coincidental projection. In seven cases, more than one optical counterpart appear to be related to an ISOCAM LW3 source. In the following analyses, we have used the "best" optical identification (i.e. , those with lowest coincidental probability), but in Table 1, we have listed all possible optical identifications with a probability within a factor two of the smallest probability.

### 3. Optical properties of the 15 $\mu\text{m}$ counterparts

### 3.1. Color and redshift distributions

The  $(I - K)_{AB}$  color distribution of the  $15\mu\text{m}$  optical counterparts (Figure 3) is significantly redder than that of the CFRS survey (top panel), with a median 0.5 magnitude redder than that of CFRS galaxies ( $\langle (I - K)_{AB} \rangle \sim 1.3$ ).

Twenty six of the sources detected at  $15\mu\text{m}$  and with  $I_{AB} \leq 22.5$  have spectroscopy available in the CFRS database. Among these are 4 stars which are also detected at  $6.75\mu\text{m}$ . Figure 4 shows the redshift histogram of ISO sources superposed on the CFRS redshift distribution. The median redshift value of the ISOCAM LW3 galaxies ( $\langle z \rangle \sim 0.76$ ) is higher than that of the CFRS ( $\langle z \rangle \sim 0.58$ ), but coincides with that of  $S_{5\text{GHz}} \geq 16\mu\text{Jy}$  radio sources (Hammer et al. 1995). Since 70% of the  $15\mu\text{m}$  optical sources have  $I_{AB} \leq 22.5$ , we estimate from the redshift distribution that more than 63% of the sources with  $S_{15\mu\text{m}} \geq 250\mu\text{ Jy}$  are at  $z \leq 1$ .

### 3.2. Spectral classifications

The spectrophotometric classification of the  $15\mu\text{m}$  optical counterparts is based on optical and emission-line properties using diagnostic diagrams and spectral templates (see Hammer et al. 1995, 1997). The following spectrophotometric types are found: fifteen emission-line galaxies, three active galaxies (including the QSO CFRS 14.0198 at  $z=1.6$ , the most distant CFRS object), one quiescent galaxy, one spiral galaxy, and one HII galaxy (CFRS 14.1103). Figure 5 shows the spectra of all extragalactic objects, classified by their spectrophotometric type.

Most (71%) of the  $15\mu\text{m}$  optical counterparts are classified as  $S + A$  galaxies, which are galaxies with moderate  $[\text{OII}]$  emission ( $W_{[\text{OII}]} \sim 20\text{A}$ ), and characterized by large

Figure 3 ; Flores et al. 1998

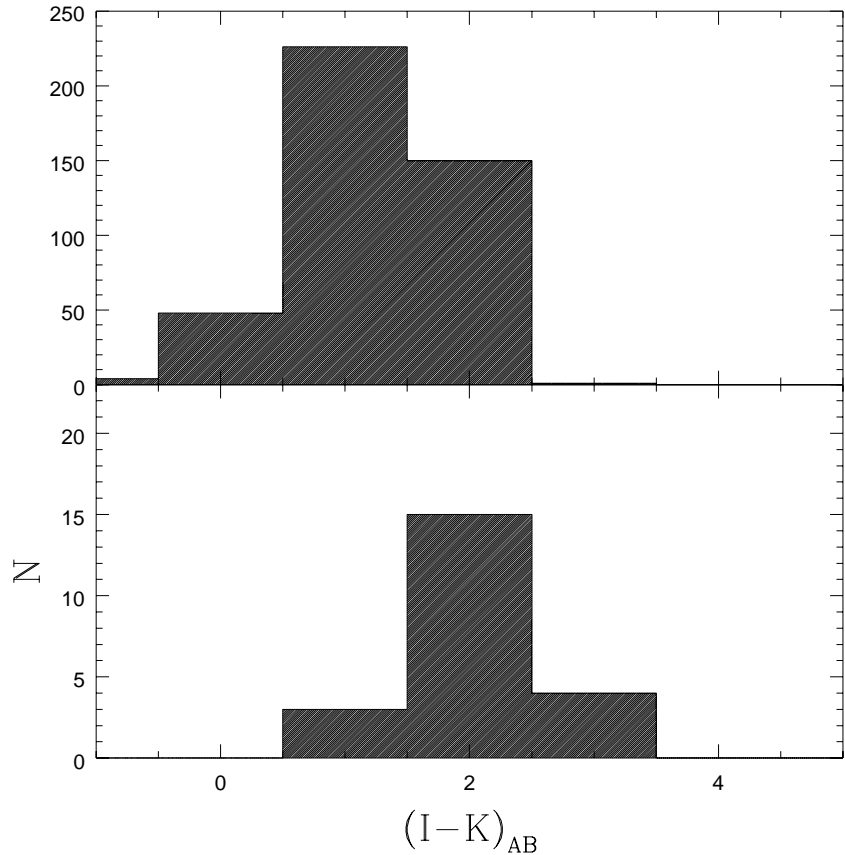


Fig. 4.—  $(I-K)_{AB}$  color distribution of  $15\mu\text{m}$  sources with  $I_{AB} \leq 22.5$  (bottom panel) compared to the CFRS galaxy color distribution (top panel).

Figure 4 ; Flores et al. 1998

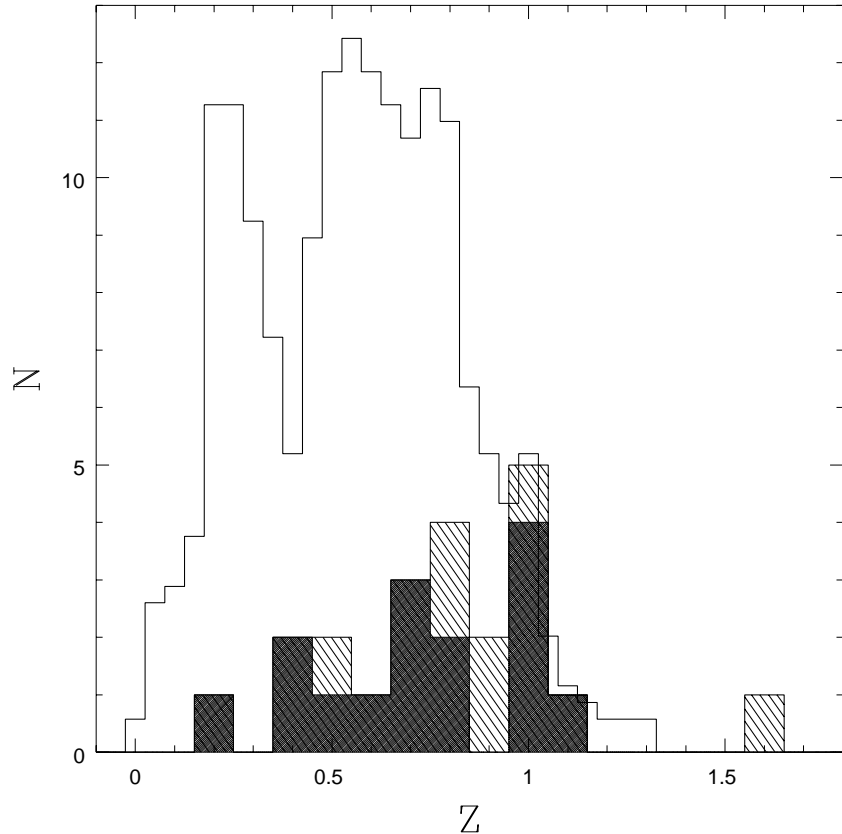


Fig. 5.— The dashed histogram shows the redshift distribution of the 22 identifications with spectra found in the CFRS database. The shaded histogram shows the redshift distribution of the sources in the catalogs 1 & 2. The non-shaded histogram shows the CFRS redshift distribution after rescaling.

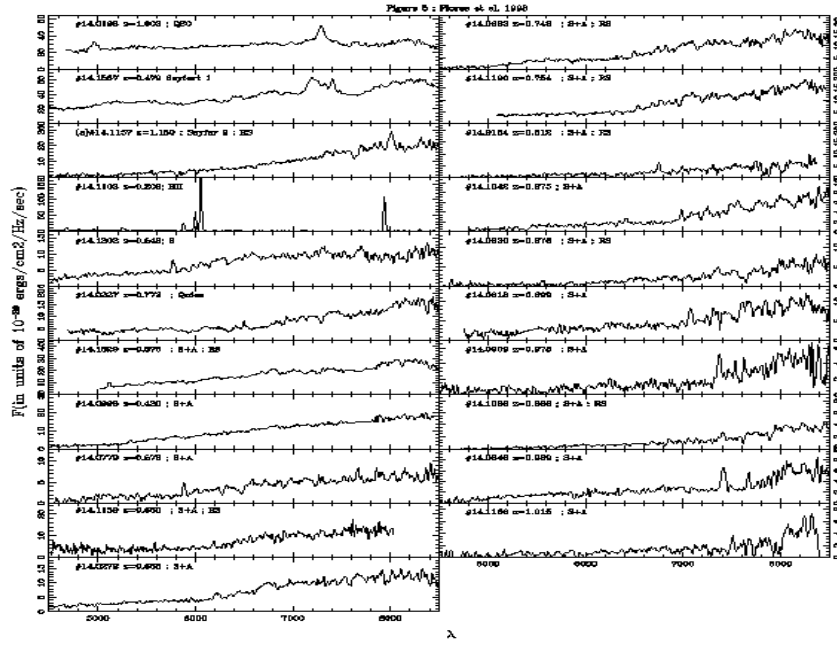


Fig. 6.— Spectral classification of the 21  $15\mu\text{m}$  sources with available spectra according to their continuum and line properties. For each object, the CFRS name, the redshift and the spectral classification are given in the upper left corner.

D(3550-3850) indices (see Table 3), as defined in Hammer *et al.* (1997). Large D(3550-3850) values can be caused by either a large A star population (D(3550-3850) is correlated with the  $H\delta$  equivalent width, D(3550-3850)=0.2 corresponding to  $W(H\delta)=5\text{-}7 \text{ \AA}$  for a non-extincted galaxy) or by very large extinctions. As we shall see, it is the A star hypothesis which is the most plausible. This suggests that in most extragalactic  $15\mu\text{m}$  sources, there were star formation occurring about 0.5 Gyr prior to the observed event. The importance of the S+A population is also supported by the fact that at high redshift, galaxies with large D(3550-3850) are also detected at  $6.75\mu\text{m}$  and at 1.44GHz.

### 3.3. Morphologies from HST and CFHT

About 30% of the CFRS field at 1415+52 has been observed by the HST. Public domain HST images of objects in the CFRS and Autifib/Low Dispersion Survey Spectrograph survey (the CFRS/LDSS deep survey, Brinchmann *et al.*, 1997) and the Groth Survey (Groth *et al.*, 1994) are available. Among the 55  $I \leq 22.5$  ISO sources with optical counterparts, 16 (30%) with have been observed with the HST F814W filter. HST images of optical counterparts of  $\mu\text{Jy}$  radio sources can be find in Hammer *et al.* (1996).

Figure 6 displays a mosaic of HST images of optical counterparts with  $I_{AB} \leq 22.5$  of  $15\mu\text{m}$  sources. For each source the CFRS name is indicated as well as its morphological classification by either Brinchmann *et al.* (1997) or us.

Two sources are unresolved by the HST (one QSO and one HII region, 14.1103). Six galaxies (37%) are found in strongly interacting systems, four (25%) are E/S0 galaxies and four (25%) are disk-dominated galaxies. Most of the 14 resolved sources show irregularities which might be interpreted as pre- or post-merging events.

Figure 6 ; Flores et al. 1998

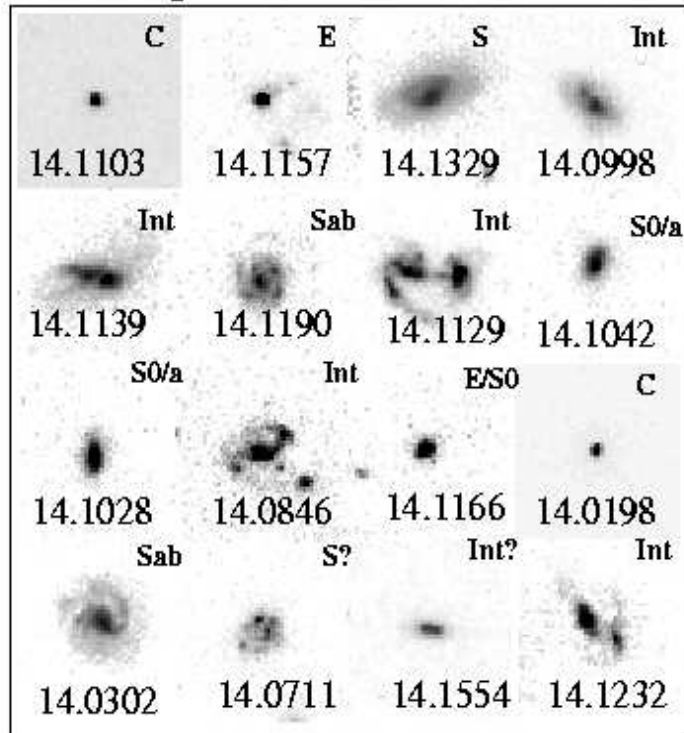


Fig. 7.— HST 5"  $\times$  5" images obtained with the F814W filter of 16 sources detected at 15  $\mu$ m with  $I_{AB} < 22.5$ . For each galaxy, the morphological classification is given in the upper right corner.

## 4. Spectral energy distributions and object classifications

### 4.1. SEDs of local galaxies: toward a template data base

Several groups have been gathering multi-wavelength observations of local galaxies (Spinoglio et al. 1995; Schmitt et al. 1998). The main limitations of the data sets are the assumed aperture corrections and possible AGN variability. SEDs of galaxies in the same class often show large differences, especially in the infrared. This is especially true for Seyfert 2 galaxies which show a wide range of colors in the near and far IR (Spinoglio et al. 1995). This large dispersion motivated us to use mean SEDs of local galaxies to compare with distant sources, so as to avoid biases for or against a given class of galaxies. For example, some Seyfert 2 galaxies may be misclassified as starbursts, but the effect on global quantities would be compensated by true starburst galaxies which are misclassified as Seyfert 2 galaxies. However average properties can be affected by a single object with extreme properties. For example, in the Schmitt et al. (1998) sample, the average radio luminosities for elliptical and spiral galaxies appears to be overestimated because of the large radio powers of NGC 1316 and of NGC 598, respectively. Indeed the mean values are significantly ( $\sim 8$  times) larger than those derived from the much larger and more complete sample of local ellipticals of Wrobel and Heeschen (1991). Using the median rather than the mean would provide a value in much closer agreement with Wrobel and Heeschen, and also provide a SED for spirals which follows the radio-far infrared correlation (Condon 1992). In the following we will use only median points for determining the SED of local templates.

Another concern is whether using local templates to analyze the properties of distant sources is appropriate. We have compared the two samples of local galaxies which have been classified and studied at several wavelengths. The Schmitt et al. sample has been mainly selected from the IUE archives and the Spinoglio et al. sample from the  $12\mu\text{m}$  faint

Figure 7; Flores et al 1998

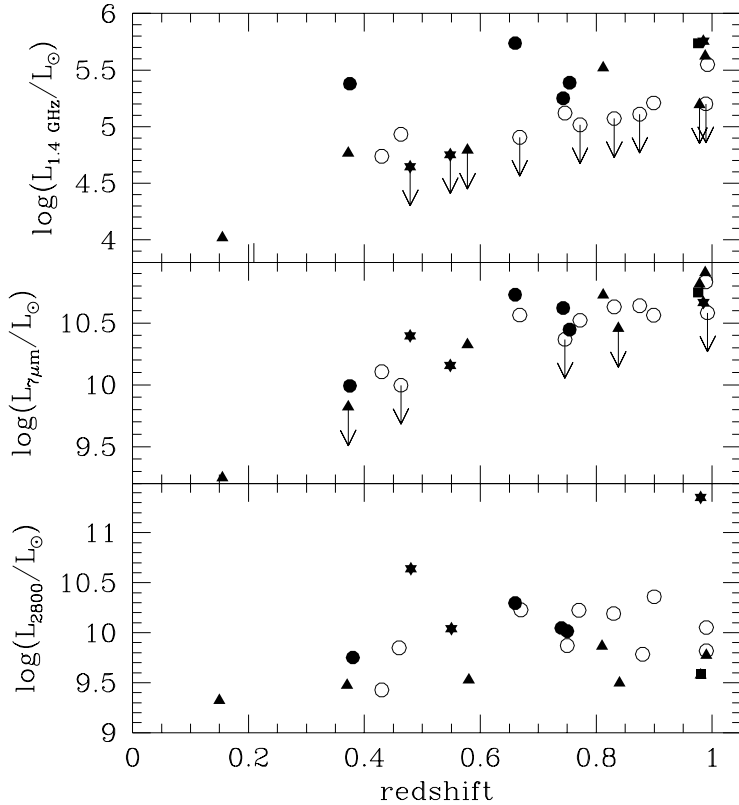


Fig. 8.— Logarithm of the luminosities at rest 1.4 GHz,  $7\mu\text{m}$  and 2800Å against redshift. Rest-frame luminosities have been interpolated from the observed luminosities at 1.4GHz and 5GHz, at 0.835, 2.2, 6.75 and  $15\mu\text{m}$ , and at 8350Å, 5500Å and 4350Å, respectively. Filled dots represent SBH, open dots S+SBH, triangles Seyfert 2 or Liner and stars QSO or Seyfert 1. Vertical arrows indicate a detection limit.

IRAS catalogue. Our 15 micron sample has been selected at the wavelengths  $15/(1+z)$  microns and  $0.835/(1+z)$  microns, so that both local samples are a priori appropriate for use as templates for our sources. The two local samples show somewhat different properties in their SEDs, especially concerning the average IR properties of Seyfert 2 galaxies. The Schmitt et al. galaxies are bright infrared galaxies and include most of the starburst and AGN templates used by Genzel et al. (1998) to compare with ultraluminous IRAS galaxies. Conversely, the Spinoglio et al. sample includes galaxies varying over a 4 to 5 magnitude range of luminosities in the infrared, and their average SEDs are mostly dominated by fainter galaxies. Figure 7 shows the distribution of luminosities for the VLA/ISOCAM/CFRS objects. Rest frame luminosities at  $7\mu$  have been interpolated from broad band observations at 0.835, 2.2, 6.75 and  $15\mu$ , and are available for most objects, except those detected only at radio wavelengths. At  $z \geq 0.5$ , these galaxies have luminosities comparable to those of the Schmitt et al. galaxies, and are 1.5 to 2.5 magnitudes brighter than the mean magnitude of the Spinoglio et al. galaxies. It is reasonable to think that the discrepancies at IR wavelengths between the Spinoglio et al. and Schmitt et al. galaxies are mainly due to the large IR luminosity differences.

The large dispersions displayed by individual Schmitt et al. galaxies in each class (especially for Seyfert 2 galaxies), ensure that this local sample is the most appropriate one for comparison with the intrinsically bright distant galaxies.

#### 4.2. Classifications of the $15\mu\text{m}$ -radio galaxies from their SEDs

According to Schmitt et al.(1997), the UV to optical range constitutes the best discriminator between Seyfert 2 and SBH or SBL (starburst with low extinction) galaxies. Seyfert 2 galaxies are generally early-type spirals, with UV colors typically bluer than those of spirals (see e.g. Kennicutt 1992). Figure 8 shows the color distribution of the radio- $15\mu\text{m}$

samples. In the (B-K, 2800Å -B) diagram, their colors are reasonably well fitted by Bruzual and Charlot (1995) models, except for three objects which are either a QSO or a Seyfert 1 galaxy. They display a range of colors which are well fitted by starburst and spiral templates. The same conclusion can be drawn from the (B-7 $\mu$ m, 2800Å -B) diagram, with a few objects having B-7 $\mu$  colors consistent with those of Seyfert 2 templates. The latter are likely to be associated with hot dust, and have redder optical-MIR colors than starbursts. In summary, most of the galaxies detected at 15 $\mu$ m have colors from the UV to the MIR consistent with those of star-forming objects: starburst and spiral galaxies.

SEDs for the 27 extragalactic 15 $\mu$ m-radio sources with  $z \leq 1$  have been constructed, using the observed fluxes at visible ( $B_{AB}$ ,  $V_{AB}$  and  $I_{AB}$  magnitudes), near-IR ( $K_{AB}$  when available), MIR (6.75 $\mu$ m, Flores et al, 1998; 15 $\mu$ m, Table 1) and radio wavelengths (1.4 GHz and 5 GHz from Fomalont *et al.*, 1985), and shifted to rest wavelengths. Each SED has then been compared to the average SED of well-known local objects (a sample of 59 galaxies, Schmitt *et al.*, 1997). The latter include E (ellipticals), Sp (spirals), SBH (highly reddened starbursts), SBL (low extinction starbursts), Seyfert 2 and LINERs. Schmitt *et al.* (1997) also provided standard deviations of the mean, which allows us to optimize the comparison.

In order to classify the SEDs, we have performed Monte Carlo simulations, assuming independent variations of our flux measurements within Gaussian error bars. In each of the 5000 Monte Carlo sets, every object SED has been fitted to template SEDs spanning all the classes defined by Schmitt et al , providing a  $\chi^2$  value weighted by the standard deviations of the mean given by those authors. Because galaxies often show properties intermediate between one class and another (see Figure 8), we also defined a hybrid class which consists

Figure 8; Flores et al 1998

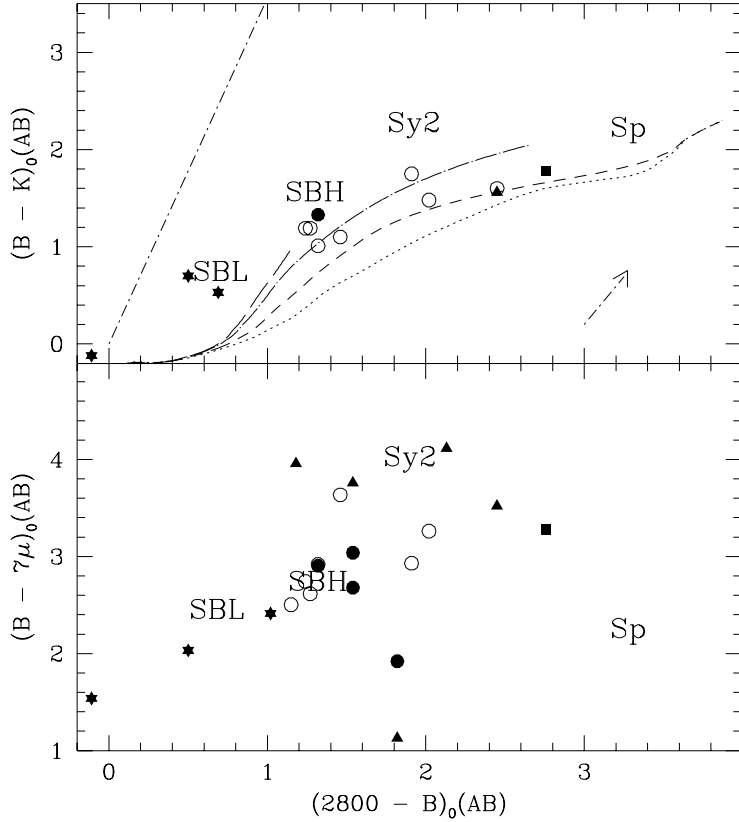


Fig. 9.— Color-color diagrams for the  $15\mu\text{m}$  and radio sources. The symbols have the same meaning as in Figure 7. In the top diagram are represented galaxies with K band photometry. In the bottom diagram, galaxies without infrared measurements are excluded. In the top diagram are shown stellar tracks from Bruzual and Charlot (1995, from top to bottom, exponentially decreasing SFR, with  $\tau=4, 1$  and  $0.5$  Gy, respectively). The dash dotted lines represents a power law and the extinction vector is indicated. In both diagrams are shown the color-color location of Schmitt et al. (1998) galaxy templates.

of a linear superposition of starburst and spiral SED templates, with the contribution of the spiral SED varying from 10% to 90% in 10% steps. This hybrid class describes the current mix of old and young stellar populations in a galaxy. We have not defined other hybrid classes such as the Seyfert 2 + starburst class, as Schmitt et al. have found that these two populations have rather similar radio to infrared properties. 27 objects were successfully classified with this technique (the averaged-weighted  $\chi$  is less than or equal to one) except for seven (Table 3). Among the latter, four are unambiguously powerful AGN as evidenced from their optical spectra (see Figure 5 and Hammer et al, 1995), including a QSO (14.1303) and Seyfert 1 galaxies (14.0573, 14.1302 and 14.1567), and one is a HII region (14.1103). The 1 sigma dispersion around the  $\chi^2$  value for each fit gives an idea of the reliability of our classification scheme (Figure 9).

#### 4.3. Final classification of the $z \leq 1$ $15\mu\text{m}$ -radio sources

Among the 27 objects selected either at radio or 15 microns, we find seven ambiguous cases, generally in the classes between Seyfert 2 and S + SBH (Table 3). Table 4 summarizes all the informations derived from their optical spectra and radio observations (spectral index and imagery). For 3 objects, emission lines or radio properties remove the ambiguity of the classification: 14.0779 shows a low ionization spectra and both 14.1028 and 14.1041 have negative radio spectral indexes and radio emission extending much beyond their optical sizes).

The validity of our classification scheme is illustrated in Figure 8, which emphasizes the relevance of the  $(B-7\mu\text{m}, 2800\text{A}-B)$  color-color diagram as a diagnostic diagram for distinguishing starbursts from AGN. In that diagram, starbursts lie in a well defined color-color region, while AGN-powered sources are around the starburst region. The object with the smallest ( $B-7\mu\text{m}$ ) color is 14.9025 which is classified as a Liner.

Figure 9 ; Flores et al. 1998

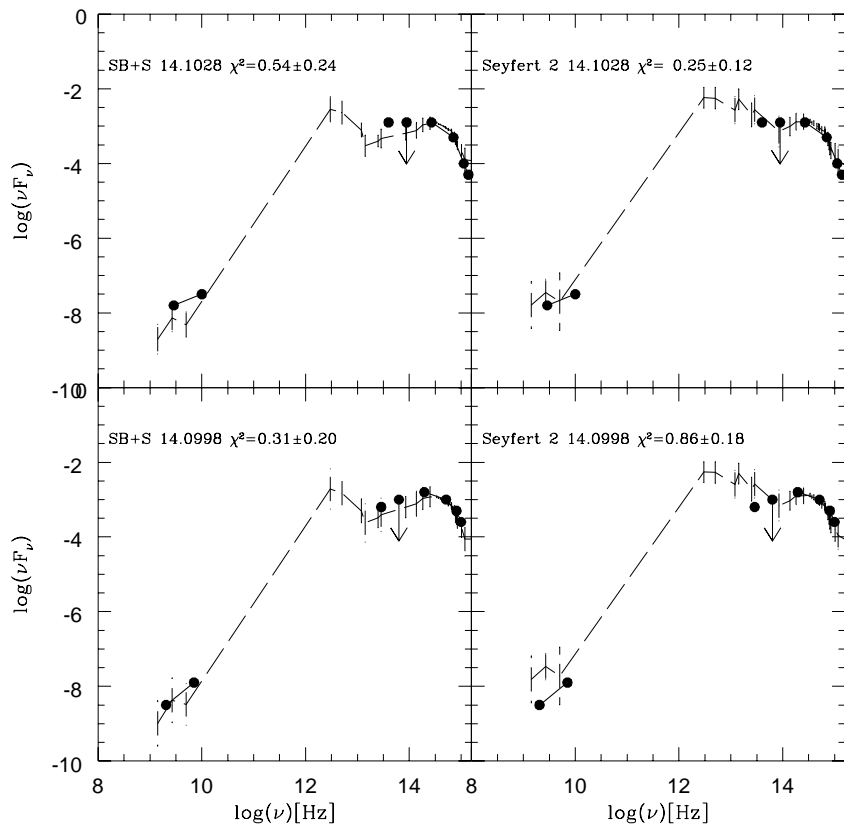


Fig. 10.— Some examples of possible ambiguous classifications of the SED. Solid dots represent flux measurements and are superposed to a template from Schmitt *et al.*. Corresponding  $\chi^2$  values are indicated (see text).

Five galaxies, all within the  $15\mu\text{m}$  sample, are classified as pure SBHs. They are generally radio sources, and were classified by Hammer et al. (1995) as being star-forming S+A objects. Figure 10 displays their SEDs on which is superposed the SBH SED from Schmitt et al. The interpolated luminosity at the  $60\mu\text{m}$  bump and the  $60\mu\text{m}$  luminosity derived from the radio-FIR correlation ( $S_{60\mu\text{m}} = 125S_{5\text{GHz}}$ , Franceschini *et al.* 1994) agree to within 20% on average. Nine objects, seven of which are in the  $15\mu\text{m}$  sample, are classified as the superposition of a starburst with a spiral SED (Figure 11). For all of them but one (14.0846), the starburst component dominates, providing more than 70% of the object bolometric luminosity (see Table 3). Only half of these objects are detected at radio wavelengths (Figure 7), so they have likely lower star formation rates than pure SBHs. It has been widely argued that powerful starbursts such as those discovered by IRAS could contain an AGN which can contribute to their infrared luminosities (Sanders et al, 1988). In addition to the fact that their energy distributions and colors are typical of those of starbursts, it is unlikely that the starbursts described here are significantly contaminated by an AGN, because:

- their infrared luminosities ( $L_{IR} < 2 \cdot 10^{12} L_\odot$ , see Table 4) are lower than those of the ultra-luminous IRAS galaxies. Local galaxies with those luminosities are mainly star-forming galaxies (Lutz et al, 1998).
- their radio spectral indices range from 0.4 to 1, between the observed frequencies of 1.4 and 5 GHz. This implies a thermal to non-thermal energy ratio in the rest frame of 0 to 0.2, in good agreement with the starburst population studied by Condon (1992).
- their radio angular sizes ( $< 2 \text{ arcsec}$ ) are always in agreement with their optical sizes, as expected if star formation was distributed over the galaxy.
- five of them have  $z \leq 0.7$  and their spectra from CFRS have [OIII]5007 and  $H\beta$  emission lines; they all show low ionization spectra, with prominent [OII]3727 line, and for all

Figure 10 ; Flores et al. 1998

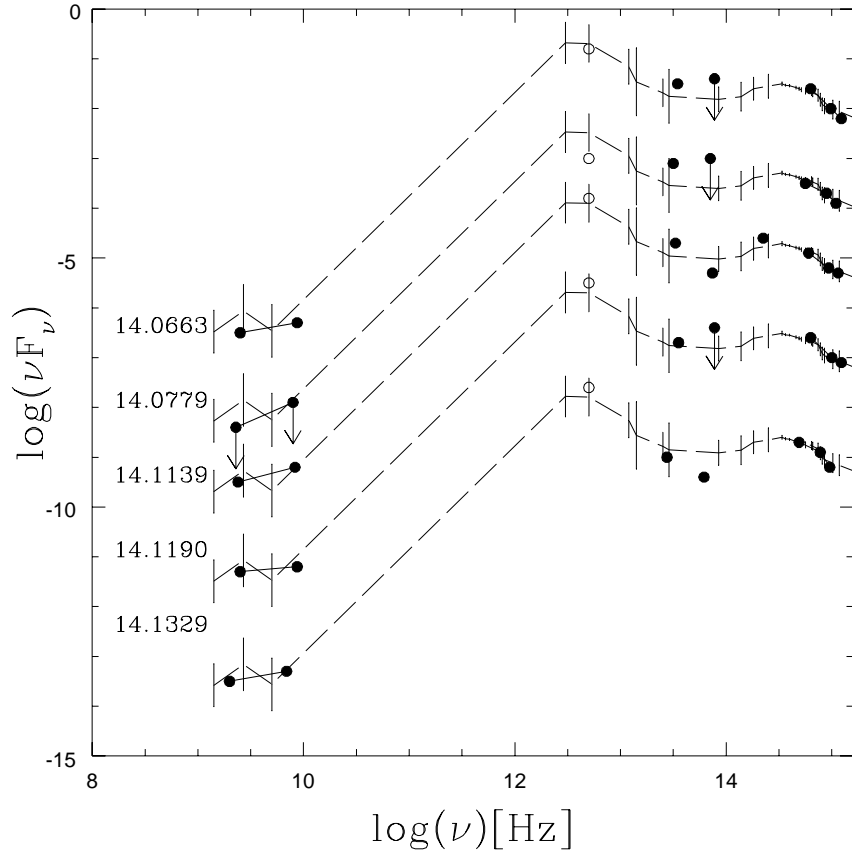


Fig. 11.— Comparison of the spectral energy distribution (SED) of 5 SBH galaxies (filled circles, separated by arbitrary vertical shifts) with a local averaged SBH SED (dashed line, from Schmitt *et al.*, 1998). Fluxes at  $60\mu\text{m}$  (open circles) are derived from radio fluxes according to the radio-FIR correlation ( $S_{60\mu\text{m}} = 125S_{5\text{GHz}}$ , Franceschini *et al.*, 1994). Superposed to the fit are vertical bars which display at each wavelength the standard deviation of the local template. The bottom panel presents the standard deviation of the 5 SBHs.

but one, no [OIII]5007 line. Figure 12 shows the sum of the five spectra, which reveals a red spectrum with  $[OII]3727/H\beta \sim 1$  and  $[OIII]5007]/H\beta \leq 0.05$ . These galaxies undoubtedly have emission-line spectra typical of HII regions, not of AGN.

Six objects, three of which are in the  $15\mu\text{m}$  sample, are classified as Seyfert 2 galaxies and four, two of which are in the  $15\mu\text{m}$  sample, are powerful AGN (Seyfert 1 and QSO). Their SEDs are shown in Figure 13 as well as that of the radio Liner 14.9025, on which are superposed Schmitt *et al.* templates or radio-quiet QSO SEDs from Sanders *et al.* (1989). The two remaining objects are 14.1103, an HII galaxy, and 14.0820, an elliptical or a spiral galaxy with moderate star formation activity ( $W_0(OII)=16\text{ \AA}$ ). The object 14.1103 ( $z=0.21$ ) is detected at  $15\mu\text{m}$  but not at radio wavelengths, and its SED is consistent with that of a local HII region. This is in agreement with the absence of an old stellar component as noted by Tresse *et al.* (1993) from the very large  $H_\alpha$  equivalent width ( $> 2500\text{ \AA}$ ). A HST image (Figure 6) shows an unresolved object, giving a diameter less than 250 pc. We are probably witnessing here a compact system undergoing one of its very first bursts of star formation:  $[OII]3727$  is not detected while  $[OIII]5007$  is very prominent. This galaxy shows spectral properties similar to those of a primordial galaxy according to Tresse *et al.* (1993). Those authors derived a low heavy-element abundance ( $\leq 0.05$  the solar value) and a large effective temperature ( $T>50\,000\text{K}$  based on the  $[OIII]4363/[OIII]5007$  ratio).

## 5. Global UV and IR luminosities

Figure 12 ; Flores et al. 1998

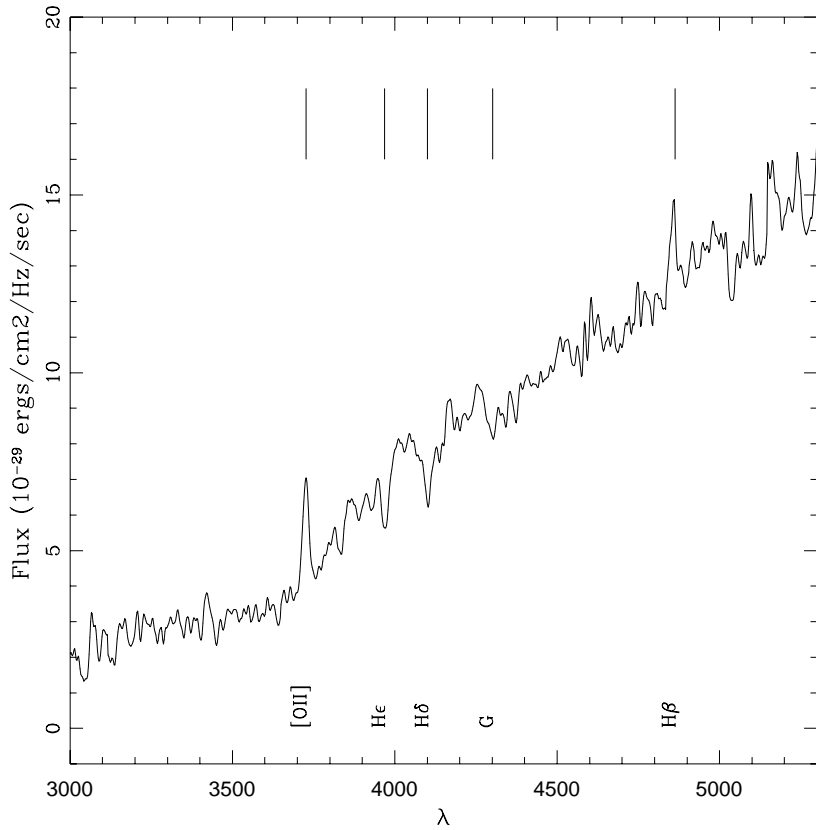


Fig. 12.— Average spectrum of the 5 SBH and S+SBH galaxies with  $z < 0.7$ . Spectral features are indicated. The average spectrum has been computed by using median values to account for luminosity variation from one object to another.

Figure 13 ; Flores et al. 1998

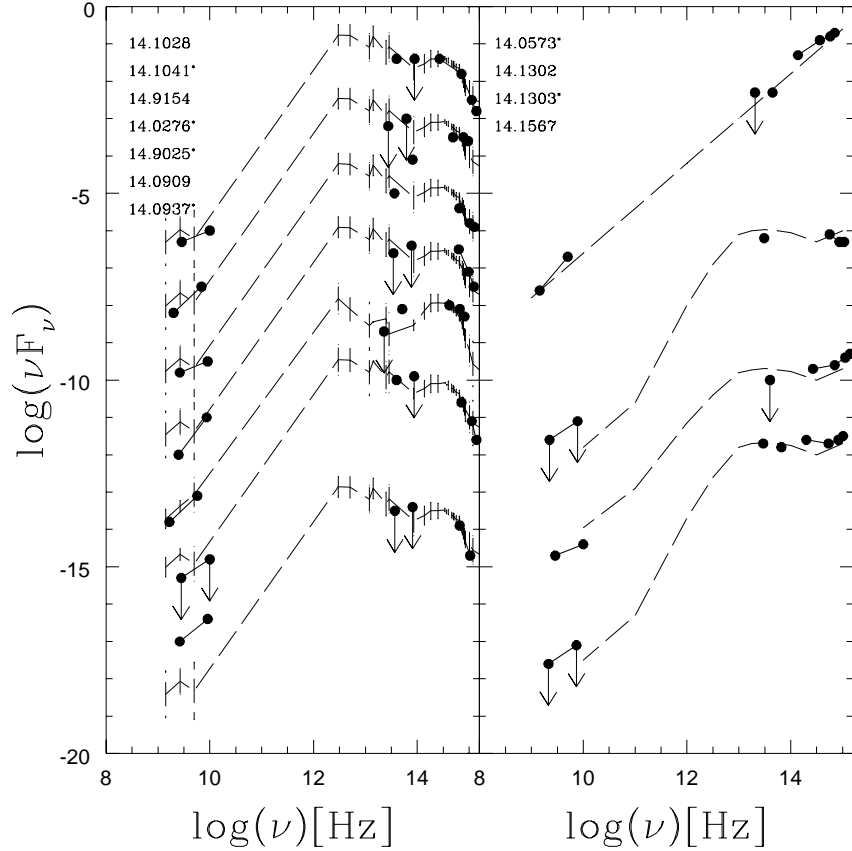


Fig. 13.— Spectral energy distributions (SED) of AGN detected with ISO at  $15\mu\text{m}$  compared with local SEDs. (left) All objects are compared with a Seyfert2 SED template except for 14.9025 (Liner SED template). (right) Powerful AGN (QSO and Seyfert1) SEDs compared with power-law or radio quiet QSO (Sanders *et al.*, 1989). Galaxies detected only at radio wavelengths are marked with an asterisk, and their fluxes at  $15\mu\text{m}$  by an arrow, assuming a upper limiting flux of  $250\ \mu\text{Jy}$ .

### 5.1. Global UV luminosity

$L_{2800}$  values have been interpolated from  $L_{4350}$  and  $(V - I)_{AB}$  (or  $(B - I)_{AB}$ ) colors, using a grid of models with exponentially decreasing SFR ( $\tau=1$  Gyr, Bruzual and Charlot, 1995) and a Salpeter IMF ( $dN(m)/dm=-2.35$  over  $m=0.1-100 M_{\odot}$ ). These calculations are found to be rather independent of the exact value of  $\tau$ , except for very small values ( $\tau << 0.1$  Gyr). We have calculated the total  $L_{2800}$  (see Table 5) in the CFRS 1415+52 field. It is based on 143 galaxies which have been spectroscopically identified and are representative of the 558  $I < 22.5$  galaxies in the field (see Lilly et al, 1995b). Converted to a luminosity density, this value is in excellent agreement (to within 6%) with that found for the whole CFRS field (Lilly et al, 1996). This is consistent with the Poisson error of 8% for the 143 representative galaxies.

### 5.2. Global infrared luminosity

#### 5.2.1. Interpolated infrared luminosities

Infrared (8-1000 $\mu$ m) luminosities are interpolated from our MIR and radio flux measurements, by using for each object the template from Schmitt et al. (1997) with the smallest  $\chi^2$ . The template gives 5 to 7 points within the wavelength range of interest, and errors can be estimated for each object using our Monte Carlo simulations. Our quoted errors take into account flux measurements errors (13% on average) as well as uncertainties in our classification scheme (5% on average). The interpolated infrared luminosity for each object along with its associated error is given in Table 4.

### 5.2.2. Global infrared luminosity from galaxies of the 15 $\mu$ m and radio samples

Galaxies detected at 15 $\mu$ m and/or at radio wavelengths have infrared luminosities in the range of  $5 \cdot 10^{10}$  to  $2 \cdot 10^{12} L_\odot$  (Table 4), comparable to those of typical local starbursts and Seyfert 2 galaxies (Genzel et al. 1998). These should be compared to their 2800 $\text{\AA}$  luminosities which range from  $4 \cdot 10^8$  to  $2 \cdot 10^{10} L_\odot$  and are not very different from those of galaxies not detected at 15 $\mu$ m and at radio wavelengths. Thus, taking into account only the UV luminosity of the 15 $\mu$ m and radio galaxies which are luminous infrared sources would lead to severe underestimates of their actual star formation rates. Nearly half of the global infrared luminosity of 15 $\mu$ m and radio galaxies is coming from 7 sources (4 SBHs and 3 Seyfert 2). These are detected at both wavelengths, except for the Seyfert 2 galaxy 14.0937. Estimates of infrared luminosities of these bright galaxies should thus not be affected strongly by source count biases or modelling uncertainties.

Accounting for the global luminosity is slightly complicated by the current observational status of the data. Hammer et al. (1995) and recent follow-up work have nearly completed the redshift identifications of the radio  $\mu$ Jy sources. Among the  $45 I_{AB} \leq 22.5$  15 $\mu$ m sources which are not detected at radio wavelengths, only 16 possess a redshift from the CFRS. The latter have not been selected *a priori* for their infrared properties, and can be considered as representative of the whole sample. In the calculation of the global luminosity, we have assumed two different scaling factors: 1 for luminous galaxies detected at radio wavelengths, and  $45/16 = 2.8$  for the less luminous galaxies undetected in radio, with an additional statistical error of 25%. Table 5 presents the different values of the global luminosities at 2800 $\text{\AA}$  and in the infrared, after excluding powerful AGN (QSO and Seyfert 1). At IR wavelengths, Seyfert 2 contribute to more than a third of the global luminosity.

### 5.2.3. *Global infrared luminosity from galaxies undetected at 15 $\mu$ m and at radio*

We consider here the subsample of the 49 galaxies which possess a redshift, are not detected at 15  $\mu$ m or radio wavelengths, and have been observed at K. This subsample can be taken as representative of the 489  $I_{AB} \leq 22.5$  galaxies not detected at 15 $\mu$ m or at radio wavelengths in the CFRS 1515+52 field. For these galaxies, we use BVIK photometry and their 15  $\mu$ m and radio upper limits to investigate their SEDs. We found that 19 of them have SEDs consistent with those of local template SEDs for SBH galaxies and 16 with local template SEDs for SBL galaxies. The relatively large fraction of SBLs (starbursts with low extinction) is compatible with the fact that they are not detected in the MIR range. Other objects have their SEDs consistent with those of local template SEDs for E/S galaxies (9 objects) or AGN galaxies (5 objects). The fraction of AGN is in reasonable agreement with Hammer et al. (1997) who find that  $\sim 8\%$  of all galaxies in the field at  $z \sim 0.5$ , are Seyfert 2 galaxies as indicated by their emission line ratios. Figure 14 displays four examples of fits for these objects. All objects but four have been reasonably classified by this method. The 4 remaining objects have been finally classified as starbursts.

### 5.2.4. *Infrared luminosity density related to star formation and uncertainties*

The luminosity density of star-forming galaxies may be simply estimated by summing up the contribution of all starburst galaxies (SBH, SBL and S+SBH) identified in the field. Uncertainties which include errors in source counts, flux errors and uncertainties in the identification, would come from our Monte-Carlo simulations.

However several complications could affect the validity of such a calculation. First, the

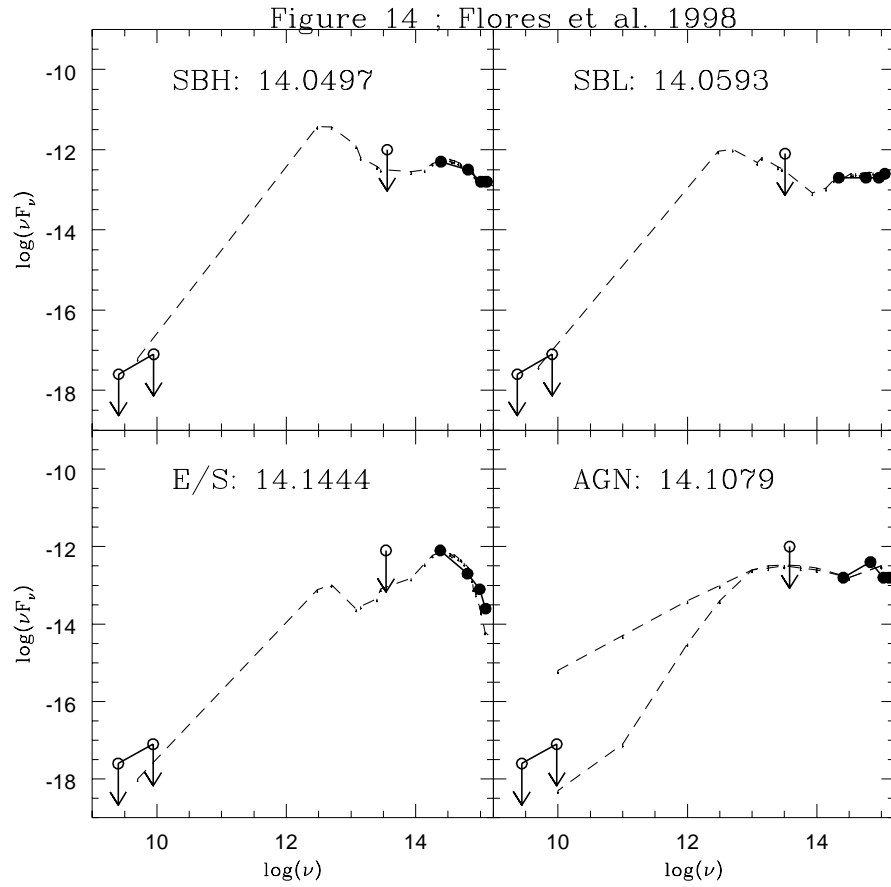


Fig. 14.— Four examples of the spectral energy distribution of galaxies which are not detected at  $15\mu\text{m}$  and at radio wavelengths, but possess B to K observations.

origin of the UV and infrared light from Seyfert 2 galaxies is unclear, and can be attributed either to the AGN or to star formation or to both. Indeed Seyfert 2 galaxies show a wide range in their infrared properties, and few color diagrams are able to distinguish them from starbursts. Contamination of the luminosity density by AGN is potentially the most serious problem for any estimate of the star formation density. Second, cirrus can contribute to the infrared luminosity, and this is likely the case for the objects classified as S+SBH. It is often assumed that the  $60\mu\text{m}$  luminosity of apparently quiescent early-type galaxies is related to cirrus excited by the emission of the underlying stellar population (Sauvage & Thuan, 1992). This is however disputed by Devereux and Hameed (1997) who present some counter-examples, and argued that young stars can be an important source of the FIR light of early-type galaxies. One may wonder however about the exact nature of early-type galaxies with a significant population of young stars embedded in dust. Might they not be equivalent to our S+SBH galaxies? In that case, the cirrus contribution to the infrared luminosity of these galaxies cannot be significant as the starburst component contribute to most of their bolometric luminosities.

Recall that former estimates of the SFR co-moving density from the UV light are uncertain, because:

1. they include contributions at  $2800\text{\AA}$  from AGN and old stellar populations.
2. they do not account for the UV light reprocessed by dust into FIR radiation.

We wish here to take into account the deficiencies mentioned above and calculate *upper and lower limits to the luminosity density related to star formation*. The upper limit is obtained with the following assumptions:

First, the  $15\mu\text{m}$  and radio fluxes of all objects not detected at those wavelengths are set equal to their detection limit. This provides an upper limit to their infrared flux.

Second, the  $2800\text{\AA}$  and  $60\mu\text{m}$  luminosities of AGN-classified objects are assumed to be powered by star formation.

Third, the infrared luminosities of S+SBH galaxies are assumed to be only coming from star formation.

The lower limit is obtained with the following assumptions:

First, all objects not detected at  $15\mu\text{m}$  and at radio wavelengths have zero extinction, and hence the star formation rate estimated at infrared wavelengths equals that estimated at UV wavelengths.

Second, the  $2800\text{\AA}$  and  $60\mu\text{m}$  luminosities of AGN and of quiescent (E) galaxies are assumed to be related respectively to the active nucleus and to the old stellar component.

Third, the infrared luminosities of S+SBH galaxies are assumed to be related to both cirrus and star formation, in the proportion of the ratio of the bolometric luminosities of the two components.

Table 5 displays the global luminosities in the CFRS 1415+52 field, as derived from UV ( $2800\text{\AA}$ ) and infrared (8-1000 $\mu\text{m}$ ) fluxes, for the sample of objects detected either at  $15\mu\text{m}$

or at radio wavelengths, and for that containing objects not detected at both wavelengths. The AGN contributions are given in the upper limit case. They can attain non negligible values ( $\sim 20\%$ ), including at UV wavelengths. This represents a major uncertainty for the SFR densities derived from UV fluxes. The errors take into account uncertainties in source counts, flux measurements errors and uncertainties in the classification scheme.

## 6. Estimation of the cosmic star formation rate

### 6.1. Star formation density derived from the UV light density

The star formation history has been estimated by various authors (see Madau *et al.* 1996; Lilly *et al.* 1996; Hammer *et al.* 1997) on the basis of the CFRS and/or the HDF surveys, using star formation rates derived from 2800Å or  $[OII]_{3727}$  fluxes. Since the UV light is dominated by emission from more or less massive stars, the total SFR as derived only from the flux at 2800Å is somewhat uncertain, as the extrapolation to the low mass end ( $M \leq 5M_{\odot}$ ) of the IMF is not constrained. Moreover Hammer *et al.* (1997) have suggested that dust and metallicity can severely affect these estimates and mask the true evolution of the cosmic star formation rate.

We adopt in the calculation of the star formation rate (SFR) from the UV light the calibration of Madau et al (1998) and Kennicutt (1998), assuming a Salpeter (1955) IMF with mass limits 0.1 and  $100 M_{\odot}$ :

$$SFR_{2800} = 5.045 \times 10^{-10} (L_{2800}/L_{\odot}) \quad (3)$$

## 6.2. Star formation density derived from the infrared light density

The SFR can also be inferred from infrared luminosities, assuming that they result mostly from dust heating by young stars, in the optically thick limit. The SFR calibration depends mainly on the burst duration and on the IMF slope at both high and intermediate mass ranges. Following Kennicutt (1998) we adopt the same IMF as that assumed to calculate the SFR derived from UV light and:

$$SFR_{IR} = 1.71 \times 10^{-10} (L_{IR}/L_{\odot}) \quad (4)$$

The above equation is based on the models of Leitherer & Heckman (1995) for a continuous burst with age 10-100 Myr. Condon (1992) calibrated the SFR from the non-thermal radio luminosity ( $L_{NT}$ ), assuming the Galactic relation between  $L_{NT}$  and the radio supernova rate. He then derived the  $SFR_{IR}$  calibration from the FIR-radio correlation, showing that  $\sim 2/3$  of the UV-optical emission is re-emitted between 40 and 120 microns (see also Helou 1988). After rescaling his value by assuming a Salpeter IMF (0.1-100  $M_{\odot}$ ), Condon (1992) obtains:

$$SFR_{IR} = 2.22 \times 10^{-10} (L_{IR}/L_{\odot}) \quad (5)$$

The difference between the two authors is at the 28% level, in agreement with the Kennicutt uncertainty estimate of  $\pm 30\%$  on his calibration, after comparison with other models (Hunter et al, 1986, Lehnert & Heckman, 1996, Meurer et al, 1997).

The key parameter in these estimations is the star formation rate of massive stars (typically  $\geq 5 M_{\odot}$ ), which are mainly responsible for the UV continuum, the non-thermal

radio continuum and FIR luminosities re-radiated by dust. The  $SFR_{IR}/SFR_{UV}$  ratio calculated in the following, is essentially independent of the IMF slope, and in particular of any extrapolation towards low stellar masses.

### 6.3. Star formation density missed by UV observations

We aim to calculate here the cosmic SFR from the infrared emission, and compare it with that derived from the UV emission. We first consider the "directly observed" SFR, based on observations of the  $I_{AB} \leq 22.5$  galaxies, as presented by Lilly *et al.* (1996). In section 5.1, we have calculated the total  $L_{2800}$  contributed by all galaxies with  $I_{AB} \leq 22.5$  and  $z \leq 1$ . In section 5.2, we have computed the total  $L_{IR}$  from those galaxies with either  $S_{15\mu m} \geq 250 \mu Jy$  or  $S_{5GHz} \geq 16 \mu Jy$  and from CFRS galaxies not detected at  $15\mu m$  and at radio wavelengths.

We have calculated the  $SFR_{IR}/SFR_{2800}$  ratio accounting for all galaxies not classified as powerful AGN. It ranges from  $2.5 \pm 0.95$  in the lower limit case, to  $5.4 \pm 1.9$  when galaxies undetected at  $15\mu m$  and in radio have their fluxes at these wavelengths equal to the detection limit. These values can however be affected by uncertainties on the calibration of the SFR in the UV and FIR wavelength ranges. Nevertheless the values we find for  $SFR_{2800}$  and  $SFR_{IR}$  show some consistency, since for all galaxies,  $SFR_{IR}$  is larger than  $SFR_{2800}$ . These ratios give extinctions ranging from  $A_V=0.49$  to  $0.87$ , if we assume a standard galactic extinction law. If the true SFR density is given by the FIR estimation, then from 35% to 85% of the global SFR co-moving density for  $z \leq 1$  are not taken into account when only the UV flux density is considered.

Figure 15 shows the co-moving SFR density evolution with lookback time (for  $H_0=50$   $\text{km s}^{-1} \text{Mpc}^{-3}$  and  $q_0=0.5$ ). The VLA-ISO-CFRS points (filled dots) represent the average values of the upper and lower limits defined above. Since there is no evidence for a change in the extinction for  $z \leq 0.5$  as compared to for  $0.5 < z \leq 1$ , we have adopted the same redshift bins as those used in previously deriving the SFR from the UV fluxes. VLA-ISO-CFRS data are  $2.9 \pm 1.3$  larger than former UV estimated values, even though latter were accounting for all sources, including strong AGN. The error bars are accounting for incompleteness errors (Lilly et al, 1996) as well as uncertainties in the determination of the SFR density at IR wavelengths.

Error bars in Figure 15 are very large mostly because we have assumed that the blue galaxies undetected at  $15\mu\text{m}$  and at radio wavelengths have no extinction (lower limit case), or have flux densities equal to the detection limits (upper limit case), both of which are clearly unrealistic assumptions. It is interesting to check whether our average value makes sense. Starbursts detected by both ISOCAM and the VLA are rare. They have large extinctions ranging from  $A_V = 1.5$  to 2, and show red continua (Figure 12). Tresse & Maddox (1998) predict an extinction of 1 mag at  $2800\text{\AA}$  (or  $A_V = 0.48$ ) for the blue field galaxy population at  $z \leq 0.3$ . If the same value holds on average for blue galaxies up to  $z = 1$ , we can predict in principle the infrared luminosity of the field galaxy population not detected at  $15\mu\text{m}$  and at radio wavelengths. For them, Table 5 gives an average value  $L_{2800} = 196 \ 10^{10} \ L_\odot$  in the field. According to equation 3, this corresponds to a global  $SFR_{2800}$  of  $980 \ M_\odot \text{yr}^{-1}$ . Adopting the Tresse & Maddox extinction estimate, the global infrared luminosity would be equal to  $1445 \ 10^{10} \ L_\odot$  (equation 4). This is in very good agreement with the average value in the fourth column of Table 5, and adds more confidence in the VLA-ISO-CFRS average values shown in Figure 15.

Figure 15 ; Flores et al. 1998

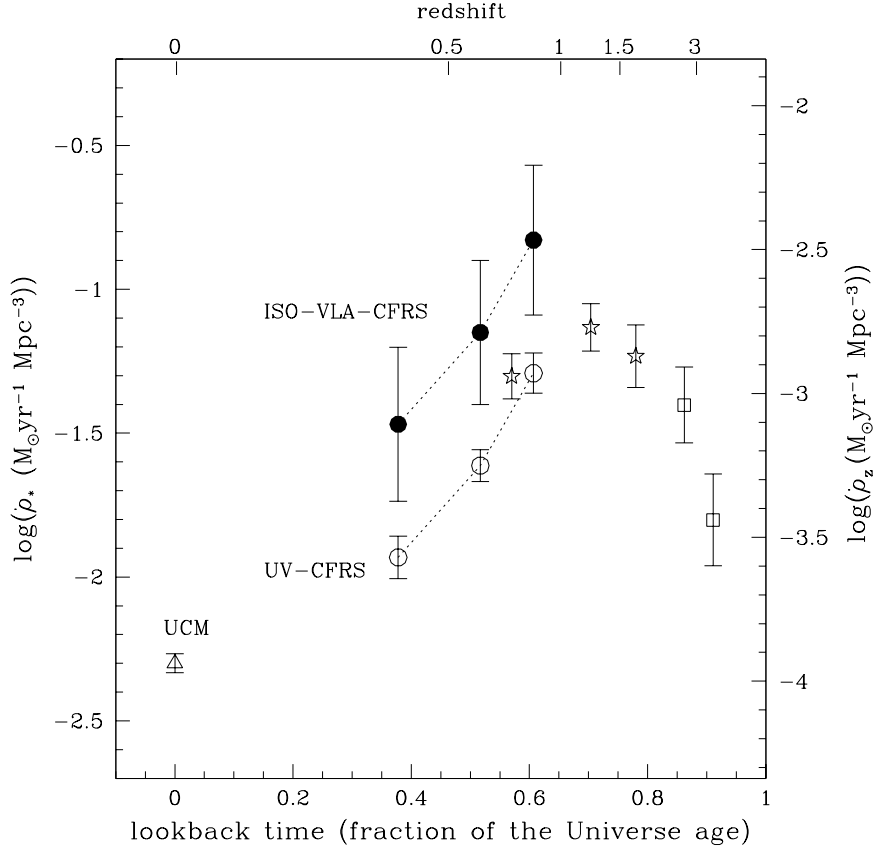


Fig. 15.— Metal production and star formation history for  $z \leq 1$  (see text). Our points (filled circles, labeled ISO-VLA-CFRS) are 2.9 times higher in SFR density or in metal production than those (open circles) previously derived from the UV flux density at 2800Å. Other points are from Gallego *et al.* (1995, open triangle), Connolly *et al.* (1997) (open stars), Madau *et al.* (1998, HDF) (open squares), and have not been corrected for extinction.

These average values imply that the stellar mass formed since  $z = 1$  would be  $3.3 \times 10^8 M_{\odot} Mpc^{-3}$ , slightly larger than the estimation of the present day stellar mass of  $3 \times 10^8 M_{\odot} Mpc^{-3}$  (Cowie et al., 1996; Glazebrook et al., 1995). Of course, the uncertainties on the SFR estimations are large, and our lower estimate is still consistent with the present day stellar mass. However we believe that this will constitute a serious problem, when uncertainties will be lowered by larger and deeper surveys at infrared and radio wavelengths. The problem gets worse if one accounts for the additional star formation at  $z > 1$ . There may be two ways out. First, half of the SFR density comes from  $\sim 10\%$  of the field galaxies, those detected at  $15\mu m$  and at radio wavelengths. These objects with large SFR (especially those with  $> 100 M_{\odot} yr^{-1}$ ) may have IMFs which significantly deviate from the Salpeter law. Alternatively, the local stellar mass density may have been systematically underestimated.

## 7. Comparison with the HDF/ISOCAM surveys

The number densities of faint MIR and radio sources found in the CFRS 1415+52 field and in the HDF appear to be a reasonable agreement. However our results are not consistent with those derived for the HDF by Rowan Robinson *et al.* (1997). The HDF is 18.5 smaller in area than the CFRS 1415+52 field, and from our results, we would expect 0.3 starburst with SFR larger than  $100 M_{\odot} yr^{-1}$ , as compared to the four starbursts with SFRs from 500 to  $1010 M_{\odot} yr^{-1}$  claimed by Rowan-Robinson *et al.* (1997). No simple explanation can account for this discrepancy of more than one order of magnitude. The calibration of the  $SFR_{FIR}$  by Rowan-Robinson et al(1997) differs slightly from ours (their proportionality factor in equation 4 is  $2.6 \cdot 10^{-10}$  instead of our  $1.7 \cdot 10^{-10}$ ). We simply stress that:

- a) our source detection and identification procedures are robust (see also Flores et al,

1998), while source identifications can be difficult in the HDF, since several galaxies in the HDF can lie within a single ISOCAM pixel.

- b)** Rowan Robinson *et al.* (1997) have used a three-component model (a stellar component giving rise to the UV to MIR emission plus cirrus and starburst components giving rise to the MIR to radio emission) to fit galaxy SEDs. This type of model has several degrees of freedom, including the relative energy ratio between the different components. The number of free parameters is larger than the number of available data points (1-3) in the MIR to radio wavelength range.
- c)** Among the twelve HDF galaxies whose SEDs were fitted by Rowan Robinson *et al.* (1997), five have limits on their radio luminosities which are significantly lower than the starburst model predictions (see their Figure 1).

Instead of force-fitting the data points by multiple-parameter starburst models, we propose here a more conservative empirical approach of fitting SEDs of galaxies with  $z \leq 1$  with SED templates of well-studied local galaxies (see Schmitt *et al.* 1997). The fits are generally quite good, especially for starburst (SB) SEDs which are consistent with the standard radio-FIR correlation. A pure starburst has its energy distribution dominated mostly by star formation. Its SED includes massive star light with or without extinction at UV wavelengths, reemission of the absorbed UV light at MIR and FIR wavelengths, and starburst thermal emission and synchrotron radiation from supernova remnants at radio wavelengths. Locally, Schmitt *et al.* (1997) show that starbursts, when compared to normal spirals or ellipticals, have a smaller spread in their SEDs from FIR to radio wavelengths. There is no evidence that these properties change significantly in the redshift range  $0 \leq z \leq 1$ .

Strong starbursts (with SFRs larger than  $70 M_{\odot} \text{yr}^{-1}$ ) should be detected by deep radio surveys to  $\mu\text{Jy}$  levels, such as those by Fomalont *et al.* (1992) in the CFRS 1415+52 field,

or by Fomalont *et al.* (1997) in the HDF. The fact that these are not detected in the HDF at radio wavelengths casts some doubts on the large SFRs derived by Rowan Robinson et al. (1997) for objects without radio counterparts. As for the 3 radio sources with  $S_{5GHz} \geq 16\mu Jy$  and  $z \leq 1$  which are found in the HDF (Fomalont et al, 1997), one (ISOHDF 12 36 46 + 62 14 06,  $z=0.96$ ) is found by Rowan-Robinson *et al.* (1997) to have the highest SFR ( $1010 M_{\odot} yr^{-1}$ ) in their sample. It is at  $z=0.96$ , has an elliptical morphology, is undetected at  $15 \mu m$  (as most of the elliptical galaxies of the Hammer *et al.* (1995) radio sample), and shows highly ionized emission typical of a Seyfert galaxy ( $MgII\lambda 2799$ ,  $[NeV]\lambda 3426$  and  $[NeIII]\lambda 3868$ ). It is likely a Seyfert 1 galaxy since the  $MgII$  line is broad, and its radio emission shows some variability (Richards et al. 1998). It is doubtful that its emission is powered by star formation.

To derive FIR luminosities (and hence SFRs) requires complete information from UV to radio wavelengths. It seems reasonable to use templates based on well-known local objects, especially for the most powerful star-forming galaxies.

## 8. Conclusions

Observations of distant field galaxies have been obtained with ISOCAM down to unprecedented flux levels at  $6.75\mu m$  ( $S \geq 150\mu Jy$ ) and at  $15\mu m$  ( $S \geq 250\mu Jy$ ). We have attempted to make our samples at both those wavelengths as complete as possible, by a careful reduction of the data. That the samples are complete is suggested by the good positional correlation between source identifications at  $6.75\mu m$ ,  $15\mu m$  and radio wavelengths.

Source densities are comparable at  $6.75\mu m$  (1944  $S > 150\mu Jy$  sources per square

degree, Flores et al. 1998),  $15\mu\text{m}$  (2808  $S > 250\mu\text{Jy}$  sources per square degree, this paper) and 5 GHz (1440  $S > 16\mu\text{Jy}$  sources per square degree, Fomalont et al, 1991). Star-forming objects contribute respectively, 50%, 73% and 26% of the extragalactic counts at  $6.75\mu\text{m}$ ,  $15\mu\text{m}$  and 5 GHz. This suggests that the  $60\mu\text{m}$  luminosity density is strongly dominated by star-forming galaxies. The fraction of  $z > 1$  objects is found to be  $< 32\%$ ,  $< 43\%$  and  $< 40\%$  of the extragalactic counts at  $6.75\mu\text{m}$ ,  $15\mu\text{m}$  and 5 GHz, respectively. The  $15\mu\text{m}$  survey is found to be rather efficient in selecting high-redshift objects, since sources with  $I_{AB} \leq 22.5$  and  $S_{15\mu} \geq 250 \mu\text{Jy}$  have a median redshift of 0.76 as compared to 0.59 for the whole CFRS.

The  $15\mu\text{m}$  survey, combined with radio and optical data, allows to identify the most powerful star-forming objects (with  $SFR$  larger than  $100 M_{\odot}\text{yr}^{-1}$ ) in the field, at least up to  $z = 1$ . Four such objects (0.7%) are found among the 578  $I \leq 22.5$  galaxies, and they contribute to 18% of the SFR density. From their UV or  $[\text{OII}]_{3727}$  emission line properties, these objects cannot be distinguished from galaxies with more modest rates of star formation. If we correct for extinction, assuming that their optical spectra from 2500 to 4000Å is reddened by the standard galactic extinction curve (with  $A_V$  derived from the  $SFR_{IR}$  to  $SFR_{UV}$  ratio), they would appear as young starbursts with a moderate population of A stars ( $W_0(H\delta) = 3.5\text{\AA}$  in the combined spectrum). The  $15\mu\text{m}$  sample contains highly reddened young starbursts as well as a larger number of galaxies (S+SB) with lower SFRs, which all contain a significant population of A stars (S+A galaxies). This is consistent with the scenario of strong starburst episodes followed by the last phases of the burst, where the IR emission is still high due to dust heating by intermediate-mass stars ( $M = 1\text{-}3 M_{\odot}$ , Lisenfeld et al, 1997).

Combination of  $15\mu\text{m}$  and radio samples probably gives a good representation of the galaxy population in a very deep  $60\mu\text{m}$  survey. Interpolated infrared (8-1000  $\mu\text{m}$ ) luminosities based on fits of galaxy SEDs by local templates from radio to UV wavelengths, imply that 75% (-40%, +10%) of the star formation rate density for  $z \leq 1$  is hidden by dust. No evidence has been found for an evolution of that fraction in the above redshift range. The global opacity of the Universe up to  $z = 1$  ranges from  $A_V = 0.5$  to 0.85. A subsample of sixteen  $15\mu\text{m}$  galaxies observed by the HST indicates that more than a third of the star formation hidden by dust is associated with interacting galaxies or mergers.

Estimates of the SFR from UV fluxes carry some uncertainties because of two main reasons, one related to the UV light reprocessed by dust into FIR radiation, and the other, to the probably important contribution of AGN light at UV wavelengths. In spite of the small statistics of the sample considered here, our work allows a first glimpse of the true SFR density for  $z \leq 1$ . From our careful data analysis, and the use of multi-wavelength data from radio to UV, we believe that the true SFR density lies within the region delimited by the still large error bars in Figure 15. Our average value, 75% of the star formation rate density hidden by dust, is consistent with:

- a one mag absorption at  $2800\text{\AA}$  for the blue galaxy population (see Tresse & Maddox, 1998), and,
- less than 4% of the galaxies are highly reddened, detected at  $15\mu\text{m}$  and at radio wavelengths and contribute to 50% of the global IR luminosity density.

Although our values are lower by a factor 2.8 than those of Rowan Robinson et al. (1997), they might be too high when the corresponding stellar mass formed since  $z = 1$  is compared to the present-day stellar mass density. This could raise an important question about the universality of the IMF, especially in the high SFR galaxies detected by ISOCAM

and the VLA, and described in this paper. Studies of other CFRS fields with the same multi-wavelength technique are needed to improve the source statistics, determine more accurately the SFR density, and study in more detail its redshift evolution.

*Acknowledgments:*

We thank Marc Sauvage and David Elbaz for useful discussions. We are also grateful to David Schade who made available the HST images of the CFRS 1415+52 field in stamp format. Comments and criticisms from an anonymous referee has led us to greatly improve the manuscript.

## REFERENCES

Brinchmann, J., Abraham, R., Schade, D., et al. ,1997, ApJ, 499, 112.

Bruzual, G. and Charlot, S. 1995.

Cesarsky, C.J., Abergel, A., Agnese, P. et al, 1996, A & AL, 315, 32.

Clements, D., Puget J., Lagache G., et al, 1998, astro-ph/9809054.

Condon, J. and Roderick J., 1988, AJ, 96, 30.

Condon, J., 1992, ARA&A **30** 575.

Connolly A., Szalay A., Dickinson M., SubbaRao M., Brunne R., 1997, ApJL, 486, 11.

Cowie, L., Hu, E. Songaila, A., and Cohen, J., 1996, ApJ, 112, 839.

Désert, F. X., Puget, J., Clements, D. L., et al. 1998, A&A, to appear.

Devereux N. and Hameed S., 1997, AJ113, 599.

Devereux N. and Young J., 1991, ApJ, 371, 515.

Edelson R. and Malkan M., 1986, ApJ, 308, 59.

Elbaz, D., Aussel, H., Baker, A., Cesarsky, C. et al, astro-ph/9807209

Flores, H., Hammer, F., Desert, F.X., et al., 1998, A&A, to appear.

Fomalont, E.B., Windhorst, R.A., Kristian, J.A. and Kellerman, K.I., 1991, AJ, 102, 1258.

Fomalont, E.B., Kellermann, K., Richards, E., et al., 1997, ApJL, 475, 5.

Franceschini A. , Mazzei P., Zotti G. and Danesse L., 1994, ApJ, 427, 140.

Franceschini A., Toffolatti L., et al, 1991, A&ASS, 89, 285.

Hammer F., Crampton, D., Lilly, S., Le Fèvre, O., Kenet, T., 1995, MNRAS, 276, 1085.

Hammer F., Schade, D., Crampton, D., Lilly, S., Le Fèvre, O., 1996, in "Science with the HST II", Proceedings of a workshop held in Paris, Dec. 4-8, 1995, ed. Benvenuti *et al*, P. 101.

Hammer F., Flores H., Lilly S., Crampton D., Le Fèvre O., Rola C., Mallen-Ornelas G., Schade D. and Tresse L., 1997, ApJ, 480, 59.

Helou G., Khan I., Malek L. and Boehmer L. 1988, ApJS 68, 151.

Hunter J. Sandford M., Whitaker R. and Klein R. 1986, ApJ 305, 309.

Genzel R., lutz D., Sturn E., el al, 1997, astro-ph/9711255.

Groth E., Kristian J., Lynds R., *et al.*, 1994, BAAS, 185, 5309.

Gallagher J., Bushouse, H., Hunter, 1989, AJ, 97, 700.

Gallego J., Zamorano, J., Aragon-Salamanca, A., Rego, M., 1995, ApJ, 455, 1.

Glazebrook K., Peacock J., Miller L., Collins C., 1995, MNRAS, 275, 169

Glazebrook K., Blake C., Economou F., et al, 1998, astro-ph/9808276.

Kennicutt, R. 1992, ApJ, 388, 310.

Kennicutt, R. Jr., 1998, to appear in ApJ, astro-ph/9712213.

Kessler M.F., Steinz, J.A., Anderegg, M.E. et al., 1996, A&AL, 315, 27.

Lehnert M. and Heckman T., 1996, ApJ 472, 546.

Leitherer M. Ferguson H. and Heckman T., 1995, AAS 186, 3004.

Lilly S., Le Fèvre O., Crampton D., Hammer F., and Tresse L., 1995, ApJ **455**, 50.

Lilly, S.J., Hammer, F., Le Fèvre, O., Crampton, D., 1995, ApJ, 455, 75.

Lilly S., Le Fèvre O., Hammer F., Crampton, D., 1996 , ApJL **460**, L1.

Lisenfeld U.,Volk H. and Xu C., 1996, astro-ph/9605118.

Lutz D., Genzel R., Rigopoulou D., et al, 1998, to appear in ApJ, astro-ph/9808330.

Madau P., Ferguson H. and Dickinson M., *et al.*, 1996, MNRAS, 283, 1388.

Madau P., Pozzetti L. and Dickinson M., 1998, ApJ, 498, 106.

Meurer G., Heckman T., Lehnert M. et al, 1997, AJ 114, 54.

Moshir M., “IRAS Faint Source Survey, Explanatory supplement” version 1, 1989.

Osterbrock, D., 1989, “Astrophysics of gaseous Nebulae and Active Galactic Nuclei”, University Science Books.

Puget J. and Léger, 1989 ARAA, 27, 169.

Puget J., Léger A. and Boulanger, F., 1985, A&AL, 142, 9.

Puget J., et al, 1998, in preparation

Richards E., Kellermann K., Fomalont E. et al, 1998, AJ 116, 1039.

Rowan-Robinson, M., Mann, R., Oliver, S., et al., 1987, MNRAS.

Salpeter E., 1955, ApJ 121, 161.

Sauvage M. and Thuau T.X., 1992 ApJL, 396, 69.

Scoville and Young J., 1983, ApJ **265** 148.

Sanders D., Soifer B., Elias J, et al, 1988, ApJ328, 35.

Sanders D., Phinney E., Neugebauer G., 1989, *et al.*, ApJ, 347,29.

Schade D., Crampton D., Hammer F., Le Fèvre, O., Lilly S.J., 1996, MNRAS, 278, 95.

Schmitt H., Kinney A., Calzetti D. and Storchi-Bergmann T., 1997, AJ, 114, 592.

Spinoglio L. and Malkan M. 1989, ESA IRSA 343.

Spinoglio L, Malkan M., Rush B. et al, 1995, ApJ 453, 616.

Tresse L., Hammer F., Le Fevre O. and Proust D. 1993, A&A 277, 53.

Tresse L. and Maddox ,1998, ApJ495, 691.

Wrobel J. and Heeschen D., 1988, ApJ, 335, 677.

Table 1. Optical counterparts of ISOCAM LW3 sources.

ISO–	$\alpha_{2000}$	$\delta_{2000}$	CFRS	$z^1$	$I_{AB}$	$V_{AB}$	$K_{AB}$	$d^3$	$P^4$	Flux <sup>5</sup>	Error
Catalogue 1: Objects with $S/N > 4$ & $P < 0.02$											
0	14:17:41.8	52:28:23.3	14.1157	1.150	20.54	22.45	–	0.65	0.000000 <sup>7</sup>	1653.	57.
5	14:17:41.9	52:30:23.2	14.1139	0.660	20.20	21.49	18.92	2.94	0.000383 <sup>7</sup>	562.	48.
9	14:17:40.4	52:28:21.1	14.1192	—	23.49	24.40	—	0.92	0.012702	399.	58.
13	14:17:52.0	52:25:32.8	14.0855	—	20.92	22.60	—	0.72	0.000998	487.	69.
32	14:17:56.6	52:31:58.6	14.0711	—	21.44	22.29	20.26	1.50	0.006552	274.	54.
42	14:18:20.9	52:25:53.0	14.0098	star	14.66	16.44	—	1.53	0.000029	362.	69.
43	14:17:42.6	52:28:46.3	14.1129	—	21.05	22.35	20.30	0.57	0.000694	209.	52.
44	14:17:34.9	52:27:51.0	14.1329	0.375	19.52	20.60	—	1.89	0.000294 <sup>7</sup>	347.	52.
51	14:17:24.3	52:30:24.0	14.1567	0.479	19.79	20.04	18.62	2.99	0.006937	459.	57.
84	14:17:45.8	52:30:31.2	14.1028	0.988	21.57	23.84	19.69	1.52	0.007463 <sup>7</sup>	295.	50.
145	14:18:07.1	52:28:37.3	14.0446	—	20.00	21.33	—	0.31	0.000089	314.	54.
206	14:18:13.4	52:31:47.3	14.0272	0.668	20.51	21.70	19.12	1.51	0.003157	297.	55.
233	14:17:58.5	52:27:14.8	14.0663	0.743	20.88	22.34	—	2.51	0.002081	288.	56.
282	14:18:18.9	52:29:05.4	14.0138	star	15.77	16.80	15.43	5.66	0.000985	214.	53.
294	14:17:47.0	52:29:11.9	14.0998	0.430	20.58	21.84	19.06	2.44	0.008694 <sup>7</sup>	245.	53.
303	14:17:46.4	52:33:50.8	14.1006	—	20.66	21.74	—	2.12	0.007003	270.	53.
308	14:17:26.7	52:32:20.9	14.1511	—	20.71	21.61	—	0.78	0.000990	284.	61.
369	14:18:4.0	52:27:47.6	14.9154	0.812	21.57	23.06	—	3.25	0.000489 <sup>7</sup>	304.	51.
Catalogue 2: Objects with $S/N > 4$ & $P(d, I) > 0.02$											
8	14:17:23.8	52:27:49.3	14.1598	—	19.84	21.00	—	8.87	0.061772	367.	73.
24	14:17:23.7	52:34:33.7	14.1582	—	22.78	23.44	—	3.92	0.123123	341.	77.
138	14:17:26.3	52:32:51.5	14.1527	—	23.00	24.24	—	5.54	0.268762	252.	62.
139	14:18:18.3	52:29:16.3	14.0150	—	22.23	24.19	19.98	1.64	0.014691	284.	57.
160	14:17:37.4	52:31:41.9	14.1278	—	22.08	28.36	20.31	11.04	0.448282	401.	55.
190	14:17:54.1	52:33:56.2	14.0779	0.578	22.01	23.10	—	2.94	0.039091	255.	53.
195	14:17:24.6	52:30:40.1	14.1569	—	20.61	21.65	19.51	7.05	0.071948	364.	61.
258	14:17:41.1	52:30:22.3	14.1166	1.015	22.46	23.88	20.46	5.24	0.166123	188.	47.
			14.1178	9.999	22.47	24.66	20.24	6.38	0.237751	188.	47.
278	14:17:42.9	52:28:00.8	14.1103	0.209	22.33	22.64	—	7.84	0.306807	235.	55.
			14.1145	—	22.64	25.72	—	7.72	0.365875	235.	55.
278			14.1091	—	22.02	22.79	—	10.70	0.412821	235.	55.
			14.1125	—	22.62	25.75	—	8.45	0.415531	235.	55.
296	14:17:56.0	52:32:55.9	14.0741	—	23.00	23.16	—	6.09	0.314943	207.	49.
			14.0743	—	21.65	22.74	—	10.58	0.320898	207.	49.

Table 1—Continued

ISO-	$\alpha_{2000}$	$\delta_{2000}$	CFRS	$z^1$	$I_{AB}$	$V_{AB}$	$K_{AB}$	$d^3$	$P^4$	Flux <sup>5</sup>	Error
304	14:17:27.3	52:32:09.6	14.1489	—	20.91	20.54	—	9.14	0.147525	284.	61.
307	14:17:47.9	52:34:06.6	14.0975	—	21.21	23.19	—	7.45	0.126166	252.	55.
325	14:18:12.5	52:32:48.4	14.0291	—	22.19	24.51	—	3.88	0.077093	225.	51.
361	14:17:49.9	52:33:43.2	14.0909	0.978	22.34	24.30	—	2.12	0.026649	248.	56.
372	14:18:02.7	52:27:59.6	14.0557	—	21.63	22.51	—	3.57	0.042434	225.	52.
421	14:17:52.5	52:35:13.4	14.9907	—	22.95	19.41	—	7.78	0.447372	259.	55.
434	14:17:44.1	52:25:50.5	14.1070	—	20.86	21.33	—	5.82	0.060281	277.	65.
440	14:17:39.3	52:28:46.1	14.1232	—	22.06	23.19	20.05	3.91	0.070782	245.	55.
440			14.1212	—	20.20	20.65	20.30	8.87	0.081572	245.	55.
457	14:17:52.1	52:30:49.8	14.0846	0.989	21.81	23.15	20.34	2.97	0.034073	250.	50.
Catalogue 3: Objects with $S/N > 4$ & without optical counterpart in $I_{AB}$											
021	14:17:23.2	52:32:58.3	—	—	—	—	—	—	1.000000	270.	62.
202	14:17:57.3	52:32:29.8	—	—	—	—	—	—	1.000000	209.	49.
288	14:17:53.6	52:33:44.6	—	—	—	—	—	—	1.000000	231.	55.
439	14:17:54.7	52:32:54.9	—	—	—	—	—	—	1.000000	248.	53.
Catalogue 4: Objects with $4 > S/N > 3$ & $P < 0.02$											
171	14:18:16.1	52:29:39.2	14.0198	1.603	20.04	20.21	19.86	1.52	0.002196	211.	56.
183	14:17:30.9	52:33:44.0	14.1400	star	15.61	16.13	—	5.59	0.000845	208.	60.
228	14:17:23.3	52:30:33.4	14.1609	star	18.93	20.83	18.30	2.54	0.002518	193.	61.
243	14:17:35.9	52:32:46.6	14.1302	0.548	20.85	21.72	—	3.19	0.018359	188.	55.
310	14:18:15.0	52:31:22.2	14.0227	0.772	20.84	22.08	19.47	3.42	0.020906	196.	53.
326	14:17:53.5	52:25:51.5	14.0818	0.899	21.02	22.14	—	2.74	0.010601	165.	54.
351 <sup>6</sup>	14:17:40.7	52:33:57.9	14.9504	—	23.90	99.99	—	8.44	0.005986 <sup>7</sup>	228.	59.
354	14:17:47.8	52:32:52.8	14.0968	—	23.39	24.88	—	1.07	0.015834	172.	54.
396	14:18:18.2	52:33:04.9	14.0151	—	17.92	18.19	—	1.93	0.000647	185.	53.
408	14:17:40.5	52:27:14.7	14.1190	0.754	20.99	22.49	—	0.95	0.001837 <sup>7</sup>	185.	56.
427	14:17:59.7	52:26:01.4	14.0645	—	22.44	24.40	—	9.72	0.000824 <sup>7</sup>	247.	67.
449	14:17:42.7	52:32:21.6	14.1117	—	20.79	21.15	—	3.77	0.024364	213.	54.
475	14:17:53.9	52:31:37.0	14.0820	0.976	21.69	24.27	19.37	11.82	0.012867 <sup>7</sup>	203.	53.
Catalogue 5: Objects with $4 > S/N > 3$ & $P > 0.02$											
137	14:17:23.9	52:25:54.1	14.1597	—	23.05	25.95	—	4.89	0.224187	284.	93.
174	14:17:45.3	52:29:47.6	14.1042 <sup>1</sup>	0.722	21.49	23.38	19.79	3.67	0.040133	197.	50.
183	14:17:30.8	52:33:54.2	14.1403	—	21.48	24.21	—	4.96	0.071532	208.	60.
228	14:17:23.7	52:30:29.7	14.1591	—	22.76	23.65	21.60	5.51	0.225442	193.	61.
243	14:17:36.0	52:32:55.4	14.1300	—	23.25	24.15	—	5.65	0.328192	188.	55.

Table 1—Continued

ISO-	$\alpha_{2000}$	$\delta_{2000}$	CFRS	$z^1$	$I_{AB}$	$V_{AB}$	$K_{AB}$	$d^3$	$P^4$	Flux <sup>5</sup>	Error
276	14:18:12.7	52:31:41.8	14.0287	—	22.29	24.19	19.98	7.56	0.281069	175.	51.
277	14:17:24.7	52:26:56.2	14.1554	—	21.90	23.07	—	5.51	0.120360	240.	76.
341	14:17:23.9	52:32:28.0	14.1576	—	22.33	23.83	—	9.93	0.444487	214.	64.
341			14.1596	—	24.21	26.44	—	4.52	0.422721	214.	64.
367	14:17:25.7	52:31:32.2	14.1533	—	22.42	23.19	21.81	7.46	0.299945	177.	54.
377	14:17:40.8	52:34:13.0	14.1170	—	21.83	23.92	—	5.14	0.100134	233.	60.
384	14:17:42.6	52:29:54.3	14.1120	—	22.60	23.57	20.78	6.25	0.251090	187.	51.
396	14:18:17.7	52:33:02.6	14.0157	—	22.35	23.01	—	7.03	0.258736	185.	53.
399	14:18:05.8	52:32:10.2	14.0477	—	23.01	24.73	—	4.36	0.177522	179.	53.
408	14:17:40.3	52:27:20.6	14.1195	—	22.67	24.42	—	5.85	0.235036	185.	56.
424	14:18:12.3	52:29:45.4	14.0302	—	20.87	22.20	19.22	5.07	0.046449	191.	50.
426	14:18:19.9	52:30:47.2	14.0112	—	23.53	24.86	20.61	6.04	0.433874	160.	53.
442	14:17:38.5	52:34:43.2	14.1252	—	21.91	21.79	—	10.02	0.347868	221.	69.
449	14:17:43.3	52:32:19.5	14.1100	—	24.46	24.37	—	2.75	0.220019	213.	54.
474	14:17:31.7	52:29:11.0	14.1393	—	22.23	23.67	21.28	2.42	0.031712	160.	52.
Catalogue 6: Objects with $4 > S/N > 3$ & without optical counterpart in $I_{AB}$											
231	14:17:33.4	52:34:21.1	—	—	—	—	—	—	1.000000	209.	59.
268	14:17:31.4	52:25:37.5	—	—	—	—	—	—	1.000000	224.	70.
348	14:18:06.3	52:25:32.0	—	—	—	—	—	—	1.000000	193.	67.
359	14:17:23.0	52:28:59.2	—	—	—	—	—	—	1.000000	234.	73.
483	14:17:29.9	52:29:21.3	—	—	—	—	—	—	1.000000	167.	53.

<sup>1</sup> The redshift for 14.1042 was given as  $z = 0.7217$  by Lilly *et al.* (1995b). “Redshifts” for the four stars (denoted by “star”) were determined from additional spectra. “—” indicates that the redshift is unknown.

<sup>2</sup> “—” indicates that the magnitude is not available.

<sup>3</sup> Distance in arcsec between ISO source and optical or radio counterpart.

<sup>4</sup> Probability that the coincidence is by chance.

<sup>5</sup> Flux within a  $9''$  aperture in  $\mu\text{Jy}$  not corrected for aperture effects (see text).

<sup>6</sup> Hammer *et al* (1995) and Fomalont *et al* (1992), comment that the fainter source ( $I_{AB} \sim 23.9$ ) galaxy, which is 2 arcsec away, should be the optical counterpart. Unfortunately, no spectrum of the fainter galaxy is available.

<sup>7</sup> Radio-source with probability based on radio source counts.

Table 2. Counts of ISO catalogs at  $15\mu\text{m}$ 

	$S/N \geq 4$	$4 > S/N \geq 3$	$S/N \geq 3$
Total	41	37	78
$\# I_{AB} \leq 22.5$	33	22	55
with z	17	9	26
$\# I_{AB} > 22.5$	4	10	14
No id	4	5	9
LW2 detection	10	7	17
radio detection	5	5	$10^1$

<sup>1</sup>Radio sources with  $S_{5GHz} \geq 16\mu\text{Jy}$ .

CFRS	E		Sp		LI NER		Seyfert2		SBL		SBH		Hybrid			Class
Hyb SB+S Clas	$\chi^2$	Er	$\chi^2$	Er	$\chi^2$	Er	$\chi^2$	Er	$\chi^2$	Er	$\chi^2$	Er	$\chi^2$	Er	%SBH+%S	
14.0227	12.69	1.24	3.18	0.59	2.47	0.81	0.97	0.27	2.21	0.78	0.37	0.31	0.19	0.13	9+1	SB+S
14.0272	12.11	1.69	4.45	0.93	2.54	0.88	1.16	0.45	1.58	0.60	0.41	0.32	0.29	0.20	8+2	SB+S
14.0276	4.22	0.31	0.75	0.22	0.75	0.18	0.51	0.17	4.10	0.85	1.32	0.20	0.15	0.12	8+2	SB+S
14.0573																Seyfert 1
14.0663	8.11	0.61	1.51	0.70	1.58	0.26	0.59	0.04	2.18	0.84	0.47	0.06	0.51	0.10	9+1	SBH
14.0727	11.90	0.95	4.07	1.25	2.89	0.38	1.41	0.30	0.70	0.30	0.55	0.16	0.23	0.19	8+2	SB+S
14.0779	16.16	2.25	21.11	18.57	6.07	1.31	0.55	0.17	1.73	0.54	0.63	0.30	1.40	0.67	9+1	Seyfert 2 /SBH
14.0818	13.20	0.89	3.0	6 0.15	4.10	0.54	1.17	0.22	2.27	2.17	0.48	0.32	0.23	0.11	8+2	SB+S
14.0820	2.94	2.21	0.62	0.19	1.69	1.85	2.13	0.22	16.92	4.31	6.59	0.99	0.64	0.26	1+9	S
14.0846	8.94	0.74	2.17	0.22	3.65	1.16	0.45	0.19	4.85	3.24	0.83	0.29	0.35	0.22	4+6	SB+S /Seyfert 2
14.0854	3.46	0.43	0.73	0.22	0.94	0.40	0.21	0.10	6.47	1.27	1.42	0.11	0.06	0.13	8+2	SB+S /Seyfert 2
14.0909	5.13	0.97	1.51	0.33	1.55	0.24	0.15	0.01	6.36	1.05	1.67	0.21	1.46	0.56	4+6	Seyfert 2
14.0937	15.61	9.20	3.63	0.72	10.81	4.20	1.53	0.16	12.68	6.98	8.53	3.37	2.79	1.11	1+9	Seyfert 2
14.0998	7.89	1.75	4.42	4.22	1.42	0.19	0.86	0.18	2.92	0.23	0.51	0.22	0.31	0.20	6+4	SB+S
14.1028	3.13	0.43	0.86	0.31	0.66	0.16	0.25	0.12	6.23	0.41	1.47	0.15	0.54	0.24	4+6	Seyfert 2 /SB+S
14.1041	23.07	6.23	33.67	72.26	6.21	1.72	1.45	0.11	1.59	0.93	7.34	3.11	1.81	1.08	8+2	Seyfert 2 /SB+S
14.1042	8.29	0.75	3.01	1.18	1.43	0.16	0.45	0.13	4.01	0.25	0.95	0.18	0.38	0.15	8+2	SB+S /Seyfert 2
14.1103																HII
14.1129	13.09	2.76	2.77	0.63	3.53	1.99	0.97	0.47	1.23	0.70	0.54	0.28	0.49	0.31	7+3	SB+S
14.1139	8.83	0.24	2.05	0.12	1.69	0.09	0.66	0.08	1.36	0.05	0.28	0.06	0.81	0.07	9+1	SBH
14.1190	8.57	0.79	1.34	0.27	1.59	0.58	0.80	0.21	2.01	0.94	0.37	0.17	0.45	0.13	9+1	SBH
14.1302																Seyfert 1
14.1303																QSO
14.1329	18.24	1.11	8.25	0.13	3.01	0.11	3.29	0.10	3.47	0.14	2.91	0.42	4.62	0.63	9+1	SBH /Seyfert 2
14.1567																Seyfert 1
14.9025																Liner
14.9154	25.58	0.27	6.54	0.18	12.43	0.23	1.52	0.08	12.15	0.23	5.43	0.12	5.47	0.19	4+6	Seyfert 2

Table 3:  $\chi^2$  values for all galaxies of the  $15\mu\text{m}$  and radio samples and classifications.

Table 5: Global Luminosities [ $10^{10} * L_{\odot}$ ] of the CFRS 1415+52 field

	15 $\mu$ m-Radio		no-detected 15 $\mu$ m -Radio		CFRS1415+52	
	L <sub>2800</sub>	L <sub>IR</sub>	L <sub>2800</sub>	L <sub>IR</sub>	L <sub>2800</sub>	L <sub>IR</sub>
Upper limit	29 $\pm$ 6	1778 $\pm$ 607	217 $\pm$ 29	2161 $\pm$ 214	246 $\pm$ 35	<b>3939<math>\pm</math>821</b>
AGN contrib.	4 $\pm$ 1	680 $\pm$ 291	17 $\pm$ 2	84 $\pm$ 27	21 $\pm$ 3	724 $\pm$ 318
”old stars” contrib	1 $\pm$ 0	115 $\pm$ 28	25 $\pm$ 3	44 $\pm$ 16	26 $\pm$ 3	159 $\pm$ 44
Lower limit	24 $\pm$ 5	984 $\pm$ 288	175 $\pm$ 24	511 $\pm$ 71	199 $\pm$ 29	<b>1495<math>\pm</math>359</b>

Table 4: Properties of the non-stellar ISOCAM LW3 and radio sources with redshift

CFRS	z	W <sub>o</sub> (OII) Å	D3538	F <sup>2</sup> <sub>7μm</sub>	F <sup>2</sup> <sub>15μm</sub>	F <sup>3</sup> <sub>5GHz</sub>	L <sup>4</sup> <sub>2800</sub>	L <sup>4</sup> <sub>IR</sub>	SFR <sup>5</sup> <sub>IR</sub>	Spec class	SED class <sup>6</sup>	α <sup>7</sup>	Ang. size <sup>8</sup>	Final class	Mor. class <sup>10</sup>
Sources detected at 15μm and at 5GHz															
Radio sources no detected at 15μm															
4.0227	0.772	0.0	0.16	<150	274	<16	1.54	31.5±7.2	54.6±20.6	Quies	SB+S	—	—	SB+S	E <sup>1</sup>
4.0272	0.668	14.3	0.20	<150	415	<16	1.54	35.9±8.6	60.3±11.4	S+A	SB+S	—	—	SB+S	C <sup>1</sup>
4.0663	0.743	4.8	0.27	<150	275	20	0.99	127.5±4.8	213.1±17.8	S+A	SBH	0.8±0.3	1.1	SBH	C <sup>1</sup>
4.0779	0.578	31.3	0.27	<150	357	<16	0.22	39.7±0.8	63.3±2.5	S+A	Seyfert 2 /SBH	—	—	SBH	C <sup>1</sup>
4.0818	0.899	22.1	0.20	<150	231	<38	2.13	50.2±5.9	86.6±10.1	S+A	SB+S	0.7±0.2	—	SB+S	C <sup>1</sup>
4.0820	0.976	16.4	0.19	<150	284	33	0.03	12.7±1.0	—	S+A	S	1.0±0.2	<1.3	S	—
4.0846	0.989	43.0	0.24	<150	350	<16	1.15	28.9±2.2	49.4±10.3	S+A	SB+S/Seyfert 2	—	—	SB+S/Seyfert 2	Int
4.0909	0.978	18.7	0.34	<150	347	<16	0.39	46.0±40.	—	S+A	Seyfert 2	—	—	Seyfert 2	C <sup>1</sup>
4.0998	0.430	11.8	0.43	<150	343	<26	0.20	5.7±0.4	10.4±5.2	S+A	SB+S	0.7±0.3	—	SB+S	E <sup>1</sup>
4.1028	0.988	18.6	0.22	<150	413	31	0.61	205.0±25.7	—	S+A	Seyfert 2/SB+S	-0.2±0.3	20	Seyfert 2	SO/a
4.1042	0.875	17.0	0.23	176	231	<16	0.28	10.1±0.8	17.3±3.0	S+A	SB+S/Seyfert 2	—	—	SB+S/Seyfert 2	SO/a
4.1103	0.209	0.0	—	<150	329	<16	0.03	1.3±0.3	HII	HII	—	—	HII	C	
4.1129	0.831	—	—	207	292	<16	1.38	26.5±2.6	45.4±13.5	—	S+SB/Seyfert 2	—	—	S+SB	Int
4.1139	0.660	19.3	0.23	161	787	79	1.38	157.5±0.5	280.6±1.8	S+A	SBH	0.5±0.1	1.9	SBH	Int
4.1190	0.754	16.0	0.30	<150	259	24	0.87	121.2±7.9	215.9±32.3	S+A	SBH	0.8±0.2	1.6	SBH	Sab
4.1302	0.548	19.7	0.14	<150	263	<16	0.86	6.5±2.5	—	S	Seyfert 1	—	—	Seyfert 1	S <sup>1</sup>
4.1329	0.375	13.5	0.18	153	485	70	0.26	62.8±3.1	112.5±10.8	S+A	SBH	0.8±0.1	0.9	SBH	SO
4.1567	0.479	0.0	-0.02	<150	642	<16	4.19	6.5±2.5	—	Seyfert 1	Seyfert 1	—	—	Seyfert 1	—
4.9154	0.812	38.7	0.34	230	425	39	0.64	130.1±11.3	—	S+A	Seyfert 2	0.3±0.2	1.5	Seyfert 2	—
4.0276	0.746	—	0.32	<150	<250	37	0.57	16.2±1.6	—	E	SB+S	<-0.4	10	Seyfert 2	—
4.0573	0.010	—	—	174	<250	37	0.57	11.1±0.5	—	Seyfert 1	Seyfert 1	-0.8±0.7	5x3	Seyfert 1	E
4.0727	0.463	32.2	0.28	<150	<250	14	0.54	11.3±2.8	19.4±3.3	S+A	SB+S	1.0±0.3	1.3	SB+S	—
4.0854	0.992	0.0	0.13	<150	<250	35	0.08	26.3±3.9	44.9±7.1	Quies	SB+S/Seyfert 2	0.0±0.3	<1.3	SB+S/Seyfert 2	SO/a
4.0937	0.838	7.6	0.04	<150	<250	1311	0.39	131.3±16.3	—	S+A	Seyfert 2	0.1±0.1	<0.2	Seyfert 2	E
4.1041	0.372	56.0	0.30	<150	<250	47	0.28	8.0±3.2	—	S+A	Seyfert 2/SB+S	-0.4±0.4	15x10	Seyfert 2	Irr
4.1303	0.985	—	—	<150	<250	46	22.20	115.7±34.7	—	QSO	QSO	0.5±0.2	<1.6	QSO	—
4.9025	0.155	—	—	243	<250	47	0.12	5.8±2.8	Liner	Liner	-0.4±0.4	15x10	Liner	Scd	

tes to Table 3:

From Shad et al. (1995).

Fluxes corrected by aperture effects in μJy.

Flux at 5GHz in μJy, from Fomalont et al. (1992).

2800 and IR (8-1000μm) luminosities in 10<sup>10</sup> L<sub>⊙</sub>.

R star formation rate in M<sub>⊙</sub>/yr.

SED classification. See table 3.

Radio spectral index, between 1.5 and 5 GHz, from Fomalont et al. (1992).

Angular size in arcsec, from Fomalont et al. (1992).

Figure 11 ; Flores et al. 1998

